

1 **Transient conduit permeability controlled by a shift between compactant shear and dilatant**  
2 **rupture at Unzen volcano (Japan)**

3

4 Lavallée Y.<sup>1</sup>, Miwa T.<sup>2</sup>, Ashworth J.D.<sup>1</sup>, Wallace P.A.<sup>1,3</sup>, Kendrick J.E.<sup>1,4</sup>, Coats R.<sup>1</sup>, Lamur A.<sup>1</sup>, Hornby  
5 A.<sup>5</sup>, Hess K.-U.<sup>6</sup>, Matsushima T.<sup>7</sup>, Nakada S.<sup>8</sup>, Shimizu H.<sup>7</sup>, Ruthensteiner B.<sup>9</sup>, Tuffen H.<sup>10</sup>

6

7 <sup>1</sup> Earth, Ocean and Ecological Sciences, University of Liverpool, Liverpool, United Kingdom

8 <sup>2</sup> Earthquake Research Department, National Research Institute for Earth Science and Disaster  
9 Resilience (NIED), Tsukuba, Japan

10 <sup>3</sup> Department of Geosciences, Environment and Society, Université Libre de Bruxelles, Brussels,  
11 Belgium

12 <sup>4</sup> Geosciences, University of Edinburgh, Edinburgh, United Kingdom

13 <sup>5</sup> Earth and Atmospheric Sciences, Cornell University, United States of America

14 <sup>6</sup> Earth and Environmental Sciences, Ludwig Maximilian University of Munich, Germany

15 <sup>7</sup> Institute of Seismology and Volcanology, Faculty of Sciences, Kyushu University, Shimabara,  
16 Nagasaki, Japan

17 <sup>8</sup> National Research Institute for Earth Science and Disaster Resilience, Tennodai, Tsukuba, 305-  
18 0006, Japan

19 <sup>9</sup> Staatliche Naturwissenschaftliche Sammlungen Bayerns (SNSB), Zoologische Staatssammlung  
20 München, München, Germany.

21 <sup>10</sup> Earth Sciences, University of Lancaster, United Kingdom

22

23

24 **ABSTRACT**

25 The permeability of magma in volcanic conduits controls the fluid flow and pore pressure development  
26 that regulates gas emissions and the style of volcanic eruptions. The architecture of the permeable  
27 porous structure is subject to changes as magma deforms and outgasses during ascent. Here, we present  
28 a high-resolution study of the permeability distribution across two conduit shear zones (marginal and  
29 central) developed in the dacitic spine that extruded towards the closing stages of the 1991-1995  
30 eruption at Unzen volcano, Japan. The marginal shear zone is approximately 3.2 m wide and exhibits a  
31 2-m wide, moderate shear zone with porosity and permeability similar to the conduit core, transitioning  
32 into a ~1-m wide, highly-sheared region with relatively low porosity and permeability, and an outer 20-  
33 cm wide cataclastic fault zone. The low porosity, highly-sheared rock further exhibits an anisotropic  
34 permeability network with slightly higher permeability along the shear plane (parallel to the conduit  
35 margin) and is locally overprinted by oblique dilational Riedel fractures. The central shear zone is  
36 defined by a 3-m long by ~9-cm wide fracture ending bluntly and bordered by a 15-40 cm wide damage  
37 zone with an increased permeability of ~3 orders of magnitude; directional permeability and resultant  
38 anisotropy could not be measured from this exposure.

39 We interpret the permeability and porosity of the marginal shear zone to reflect the evolution of  
40 compactional (i.e., ductile) shear during ascent up to the point of rupture, estimated by Umakoshi et al.  
41 (2008), at ~500 m depth. At this point the compactional shear zone would have been locally overprinted  
42 by brittle rupture, promoting the development of a shear fault and dilational Riedel fractures during  
43 repeating phases of increased magma ascent rate, enhancing anisotropic permeability that channels fluid  
44 flow into, and along, the conduit margin. In contrast, we interpret the central shear zone as a shallow,  
45 late-stage dilational structure, which partially tore the core of the spine, leaving a slight permanent  
46 displacement. We explore constraints from monitored seismicity and stick-slip behaviour to evaluate  
47 the rheological controls, which accompanied the upward shift from compactional toward dilational  
48 shear as magma approached the surface, and discuss their importance in controlling the permeability  
49 development of magma evolving from overall ductile to increasingly brittle behaviour during ascent  
50 and eruption.

51

## 52 **1. Introduction**

### 53 *1.1. Outgassing pathways and volcanic eruptions*

54 The style and timing of activity exhibited during a volcanic eruption are strongly influenced by  
55 the presence and mobility of volatiles in magma (Sparks, 1997; Woods and Koyaguchi, 1994) and  
56 surrounding conduit wallrock (Jaupart and Allègre, 1991). During magma ascent, volatiles are exsolved  
57 into gas bubbles (Navon et al., 1998; Sparks, 2003) as their solubility decreases with decompression  
58 (Liu et al., 2005), crystallisation (Tait et al., 1989), and heat generated by crystallisation (Blundy et al.,  
59 2006) and shear (Lavallée et al., 2015). This causes the accumulation of pressurised fluids in vesicles  
60 that charges ascending magma, which, if sufficient may lead to fragmentation (Mueller et al., 2008;  
61 Alidibirov and Dingwell, 1996) and an explosive eruption (Sahagian, 1999). The development of a  
62 permeable network governs outgassing (Edmonds et al., 2003), pore pressure release (Mueller et al.,  
63 2005), and eruptive cyclicality (Michaut et al., 2013), thereby reducing the potential for explosive activity  
64 (Klug and Cashman, 1996) and encouraging effusion (Edmonds and Herd, 2007; Eichelberger et al.,  
65 1986; Degruyter et al., 2012). Lava dome eruptions—the topic of this study—commonly switch  
66 between effusive and explosive modes of activity due to this competition between permeability, pore  
67 fluid pressure and the structural integrity of magma (Melnik and Sparks, 1999; Calder et al., 2015;  
68 Cashman et al., 2000; Castro and Gardner, 2008; Edmonds et al., 2003; Lavallée et al., 2013; Lavallée  
69 et al., 2012; Sparks, 1997; Holland et al., 2011; Kendrick et al., 2016; Platz et al., 2012). Considering  
70 the water solubility-pressure relationships in magmas (Zhang, 1999), permeability-porosity  
71 relationships in magma (Westrich and Eichelberger, 1994) and eruptive patterns (Edmonds et al., 2003),  
72 it has been suggested that much of the outgassing during lava dome eruptions occurs in the upper few  
73 kilometres of the conduit (Westrich and Eichelberger, 1994; Edmonds et al., 2003). This observation is  
74 corroborated by rapid shallowing of seismicity leading to explosions (e.g., Rohnacher et al., 2021) and  
75 the existence of shallow long-period seismic signals resulting from resonance in fractures and faults  
76 (Chouet, 1996; Matoza and Chouet, 2010) as fluids are channelled to the surface (Holland et al., 2011;  
77 Kendrick et al., 2016; Gaunt et al., 2014; Nakada et al., 1995; Newhall and Melson, 1983; Pallister et  
78 al., 2013b; Sahetapy-Engel and Harris, 2009; Sparks, 1997; Sparks et al., 2000; Edmonds et al., 2003;  
79 Varley and Taran, 2003; Stix et al., 2003). Therefore understanding the evolution of the permeable  
80 network during eruptive shearing is central to constrain the evolution of the magmatic system in the  
81 shallow crust (Blower, 2001).

82 Close examination of the architecture of shallow dissected conduits and structures in vent-  
83 proximal silicic lava exposes complex shearing histories that would impact the permeable porous

84 network of erupting magma. These structures reveal porosity contrasts through the lavas, and strain  
85 localisation near the conduit margins is commonly identified via the presence of flow bands and variably  
86 porous shear zones with a spectrum of configurations (Gaunt et al., 2014; Kendrick et al., 2012;  
87 Kennedy and Russell, 2012; Pallister et al., 2013a; Smith et al., 2001; Stasiuk et al., 1996; Tuffen and  
88 Dingwell, 2005); features that are preserved to differing extents in crystal-poor and crystal-rich magmas  
89 (Calder et al., 2015; Lavallée and Kendrick, 2021). For example, crystal-poor obsidian in dissected  
90 conduits and dykes commonly exhibits marginal flow bands, showing alternation between glassy, finely  
91 crystalline and microporous bands (Gonnermann and Manga, 2007). Flow bands also occur as variably  
92 sintered, cataclastic breccia layers, resulting from fracture and healing cycles (Tuffen and Dingwell,  
93 2005; Tuffen et al., 2003), and as variably sintered tuffisite layers, resulting from fragmentation and  
94 entrapment of fragments into narrow fractures (Castro et al., 2012; Heiken et al., 1988; Kendrick et al.,  
95 2016; Kolzenburg et al., 2012). Exposed crystal-poor conduits, dykes and domes are commonly dense,  
96 as the porous network may easily collapse (unlike crystal-rich lavas; e.g., Ashwell et al., 2015). The  
97 collapse of the porous network occurs as eruptions wane and pore pressure is insufficient to counteract  
98 surface tension and local magmatic and lithostatic stresses (Kennedy et al., 2016; Wadsworth et al.,  
99 2016), a process which hinders interpretation of the syn-eruptive permeable structure of crystal-poor  
100 magma from the study of large-scale relict formations. Studies of erupted crystal-poor pumices (which  
101 quench rapidly) help provide constraints on the extent of magma permeability at the point of  
102 fragmentation (Wright et al., 2006), but the task of reconstructing the permeable architecture of an entire  
103 conduit from these pyroclasts is challenging (Dingwell et al., 2016), further complicated by post-  
104 fragmentation vesiculation (Browning et al., 2020) and vesicle relaxation (Rust and Manga, 2002), and  
105 so remains to be attempted systematically.

106 Crystal-rich volcanic rocks (the subject of this study) expose a wider range of permeable porous  
107 structures (Farquharson et al., 2015; Mueller et al., 2005; Klug and Cashman, 1996; Lamur et al., 2017;  
108 Kushnir et al., 2016)(Ryan et al., 2020). These rocks frequently share common characteristics and  
109 evidence that crystal-rich magmas preferentially shear and accumulate damage near the conduit  
110 margins, defined by flow bands and/ or cataclastic fault zones, adjacent to brecciated wall-rocks (Sparks  
111 et al., 2000; Hale and Wadge, 2008; Watts et al., 2002). For instance, dacitic volcanic spines extruded  
112 in 2004-08 at Mount St. Helens (USA) and in 1994-95 Unzen volcano (Japan) reveal the presence of a  
113 complex ‘damage halo’ near the conduit margin (Calder et al., 2015; Gaunt et al., 2014; Pallister et al.,  
114 2013a; Smith et al., 2001; Kendrick et al., 2012; Wallace et al., 2019). Shear zones at Mount St. Helens  
115 (Gaunt et al., 2014) and at Chaos Crags, Lassen volcano (Ryan et al., 2020), showed increased porosity  
116 and permeability, and the development of permeability anisotropy towards the conduit margin, thus  
117 describing scenarios in which shearing of dense, crystal-rich magma induced dilation. In the case of  
118 Mount St. Helens, in the later Spine 7, the fault zone is defined by the presence of a pseudotachylyte  
119 (Kendrick et al., 2012), a feature which can reduce the permeability of shear zones in magmas (Kendrick  
120 et al., 2014a). At Unzen volcano, Smith et al. (2001) qualitatively described the character of the shear  
121 zone developed in the centre of the lava spine at Mount Unzen, highlighting the presence of a dilational  
122 cavity associated with shearing in the core of the magmatic column. However, they did not quantify  
123 any porosity-permeability relationships. The cavity (hereafter termed “central shear zone”) was defined  
124 by an area in which the groundmass was torn, producing pore spaces in the shadow of phenocrysts. The  
125 margin of the Unzen spine also hosts a spectrum of shear textures (Hornby et al., 2015; Wallace et al.,  
126 2019), and significant low-frequency seismicity during the eruption indicated flushing of fluids in the  
127 marginal fault zone (Lamb et al., 2015). Thus, the study of evolving monitored signals and eruptive  
128 products at Unzen depicts a wide range of outgassing pathways, which evolve during the course of  
129 magma ascent and lava dome eruptions.

130

131 1.2. *The permeability of magmas and rocks*

132 Several studies have explored the permeability evolution of volcanic materials, but due to the  
133 occurrence of many influential structural and petrological processes in shallow volcanic conduits, no  
134 solutions yet encompass the complete history of magma permeability during volcanic eruptions:  
135 especially its time- and strain-dependent evolution. Following nucleation and growth, bubbles interact  
136 and coalesce beyond a certain vesicularity, termed the percolation threshold, promoting the onset of  
137 fluid flow through a connected bubble network (Baker et al., 2012; Eichelberger et al., 1986; Rust and  
138 Cashman, 2004; Burgisser et al., 2017). The porosity of the percolation threshold varies widely  
139 (between ~30 vol. % and 78 vol. % bubbles) depending on the size and geometry distributions of the  
140 bubble population (Colombier et al., 2017; Rust and Cashman, 2004; Burgisser et al., 2017).  
141 Vesiculation experiments have shown that permeability remains low in isotropically vesiculated  
142 (aphyric and crystal-bearing) magmas as percolation initiates at vesicularities higher than those  
143 theoretically predicted (Okumura et al., 2012; Okumura et al., 2009). Yet, bubble coalescence may be  
144 accentuated by transport processes such as the thinning or draining of melt along the bubble wall (Castro  
145 et al., 2012), deformation (Ashwell et al., 2015; Kennedy et al., 2016; Okumura et al., 2010; Okumura  
146 et al., 2006; Okumura et al., 2008; Wadsworth et al., 2017; Shields et al., 2014; Farquharson et al.,  
147 2016b; Kendrick et al., 2013), and rupture (Lamur et al., 2017; Lavallée et al., 2013; Heap and Kennedy,  
148 2016; Okumura and Sasaki, 2014; Heap et al., 2015a; Laumonier et al., 2011), or lessened by fracture  
149 infill (Kendrick et al., 2014a; Kendrick et al., 2016; Wadsworth et al., 2016), all of which influence the  
150 permeability of magma and promote permeability anisotropy (Farquharson et al., 2016c) during its  
151 prolonged ascent to the Earth's surface.

152 In recent decades, laboratory measurements have helped us gain a first order constraint on the  
153 permeability-porosity relationships of volcanic products (Eggertsson et al., 2018; Mueller et al., 2005;  
154 Acocella, 2010; Rust and Cashman, 2011; Colombier et al., 2017; Farquharson et al., 2015; Klug and  
155 Cashman, 1996). These suggest a non-linear increase of permeability with porosity; yet, depending on  
156 the nature of the porous network, influenced by eruptive history, the permeability of rocks with a given  
157 porosity may range by up to 4-5 orders of magnitude. Controlled laboratory experiments have given us  
158 insights on probable permeability trends of magma subjected to different stress, strain, and temperature  
159 conditions (Ashwell et al., 2015; Kendrick et al., 2013; Lavallée et al., 2013; Okumura et al., 2012;  
160 Okumura et al., 2006; Shields et al., 2014), but a complete description of the dynamic permeability of  
161 deforming magma requires *in-operando* determination under controlled conditions, which remain  
162 scarce (Gaunt et al., 2016; Kushnir et al., 2017b; Wadsworth et al., 2017; Wadsworth et al., 2021); these  
163 studies have shown that surface tension and/or low-strain rate conditions under positive effective  
164 pressure (*i.e.*, confining pressure greater than pore pressure) promote compaction and reduce  
165 permeability. These informative descriptions require further inputs to enable robust relationships with  
166 magma rheology, influenced by the presence and configuration of bubbles. Shallow magmas contain  
167 bubbles and crystals and exhibit a non-Newtonian rheology (Caricchi et al., 2007; Lavallée et al., 2007;  
168 Lejeune et al., 1999; Lejeune and Richet, 1995; Kendrick et al., 2013; Coats et al., 2018) that favours  
169 the development of strain localisation, in particular, by preferentially deforming pore space (Kendrick  
170 et al., 2013; Okumura et al., 2010; Shields et al., 2014; Pistone et al., 2012; Mader et al., 2013) As  
171 magma shears, the porous network adopts a new configuration reflecting the stress conditions and  
172 magma viscosity (Rust et al., 2003; Wright and Weinberg, 2009), which influences the permeability  
173 (Ashwell et al., 2015; Kendrick et al., 2013; Okumura et al., 2010; Okumura et al., 2009; Okumura et  
174 al., 2006; Okumura et al., 2008; Okumura et al., 2013). Shearing may increase or decrease the porosity  
175 and permeability depending on the applied stress, strain and porosity of the deforming material and  
176 direction of the permeability measurement due to the development of anisotropy (Ashwell et al., 2015;  
177 Kendrick et al., 2013). In cases of extreme shear, magma may rupture, thereby increasing pore



178 connectivity and permeability (Laumonier et al., 2011; Lavallée et al., 2013; Okumura et al., 2013) until  
179 the fracture heals via diffusion (Okumura and Sasaki, 2014; Tuffen et al., 2003; Lamur et al., 2019;  
180 Yoshimura and Nakamura, 2010), seals via secondary mineralisation (Heap et al., 2019; Ball et al.,  
181 2015), or infills with tuffisitic material (Castro et al., 2012; Kendrick et al., 2016; Kolzenburg et al.,  
182 2012; Tuffen and Dingwell, 2005), which may densify through time (Kendrick et al., 2016; Vasseur et  
183 al., 2013; Wadsworth et al., 2014; Farquharson et al., 2017). The densification of magma under isotropic  
184 stresses (due to surface tension) has been reconstructed using high-resolution x-ray computed  
185 tomography from synchrotron imaging, providing us with a first complete description of magma  
186 permeability evolution as a function of porosity. This indicates that densification intrinsically relates to  
187 the evolution of the size distribution and surface area of the connected pore space (Wadsworth et al.,  
188 2017; Wadsworth et al., 2021). Nonetheless, a time- and strain-dependent description of the  
189 development of the porous network of shearing magma remains incomplete, and information must be  
190 sourced from our understanding of permeability evolution in deforming rocks.

191 In rock physics, the evolution of the porous network in deforming rocks has been extensively  
192 studied. In its simplest description, the modes of deformation differ at low and high effective pressures  
193 as rocks adopt brittle or ductile behaviour, respectively. These are defined as a macroscopic behaviour  
194 (not a mechanistic description), whereby ‘brittle’ refers to the localisation of deformation leading to  
195 rupture, and ‘ductile’ refers to the inability for rocks to localise strain during deformation (e.g., Rutter,  
196 1986); see Lavallée and Kendrick (2020) and Heap and Violay (2021) for reviews of brittle and ductile  
197 deformation in volcanic materials. The key distinction between these two deformation modes is that  
198 brittle failure generally results in local dilation (i.e. the creation of porosity), whereas ductile  
199 deformation results in compaction of the porous network (Heap et al., 2015a). As a result, brittle  
200 (dilatational) failure generally enhances the permeability of rocks (Heap and Kennedy, 2016; Lamur et  
201 al., 2017; Farquharson et al., 2016b), whereas ductile (compactional) deformation generally causes  
202 reduction in permeability (Heap et al., 2015a; Loaiza et al., 2012), though there are exceptions. Despite  
203 its crucial role in defining deformation mode in rock, the role of effective pressure in dictating the  
204 ductile and brittle modes of deformation has not been systematically mapped out for multiphase  
205 magmas; instead, we generally consider the effects of temperature and applied stress or strain rate (e.g.,  
206 Lavallée et al., 2008) over that of stress distribution, as the deformability of magma imparts technical  
207 challenges to classic rock mechanic tests and permeability determination (Kushnir et al., 2017b). We  
208 may thus anticipate some similarities between rock and magma deformation modes, whereby: At high  
209 effective pressure, ductile deformation is favoured via compactant viscous flow or even cataclastic flow  
210 (if strain rates are high enough to cause pervasive fracturing of bubble walls), causing porosity and  
211 permeability reduction; at low effective pressure, viscous flow may promote compaction at low strain  
212 rates, whereas dilation may ensue if strain rate favours localised rupture (Lavallée and Kendrick, 2020).  
213 Similarly, embrittlement may take place if a porous magma efficiently compacts, shifting its properties  
214 from the ductile to brittle regime (Heap et al., 2015a). Across this viscous-brittle transition, magma  
215 rupture may be partial and end abruptly, leaving a blunt fracture tip (Hornby et al., 2019). Most, if not  
216 all, of the features observed in experimentally deformed rocks and lavas should be observable in a  
217 shallow magmatic system, hinging on a delicate balance between ductile and brittle deformation  
218 regimes; these would influence outgassing, prompting temporal and spatial variations in effective  
219 pressure. In this study, we examine the well-preserved, dacitic lava spine erupted in 1994-95 at Unzen  
220 volcano to constrain the permeability of dilatational and compactional shear zones that developed in the  
221 shallow volcanic conduit.

222

223 *1.3. 1990-1995 eruption of Unzen volcano*

224 Unzen volcano is a stratovolcano located near the city of Shimabara on the island of Kyushu,  
225 Japan (Fig. 1). The volcano underwent a 5-year period of protracted dome growth which threatened the  
226 surrounding population with the occurrence of several thousand rockfalls and many pyroclastic flows,  
227 such as the destructive event on 3<sup>rd</sup> June 1991 that caused 43 fatalities. Activity initiated in early 1990  
228 with a series of phreatic explosions and brief extrusion of a spine on 19<sup>th</sup> May; this was swiftly followed  
229 by continuous growth of a lava dome until early 1995 (Nakada et al., 1995). Between October 1994 and  
230 January 1995, the eruption concluded with the extrusion of a spine through the dome surface (Fig. 1c).  
231 At the dome surface, gas emissions focused along the spine marginal faults (Ohba et al., 2008). The  
232 dome products have a dacitic composition and contain euhedral phenocrysts of plagioclase and  
233 amphibole in a groundmass containing microlites of plagioclase, amphibole, pyroxene and iron oxides  
234 (Nakada et al., 1995; Wallace et al., 2019). Petrological constraints suggest that degassing initiated at a  
235 pressure of approximately 70-100 MPa; *i.e.*, in the upper ~3-4 km depth (Nakada et al., 1995).

236 Dome growth occurred in stages, forming thirteen discrete lobes until mid-July 1994. Growth  
237 was observed to be typically exogenous when effusion rates were high, and endogenous at effusion  
238 rates lower than  $2.0 \times 10^5 \text{ m}^3 \text{ d}^{-1}$  (Nakada et al., 1999). In five years, the eruption generated  $2.1 \times 10^8 \text{ m}^3$   
239 of lava at an average ascent rate estimated at 13–20  $\text{md}^{-1}$  (Nakada et al., 1995); the final spine extruded  
240 from late-1994 to early-1995 at a rate of approximately 0.8  $\text{md}^{-1}$  (Yamashina et al., 1999). The rheology  
241 of the erupted dome lavas has been a source of debate (Goto et al., 2020; Sato et al., 2021), as it is  
242 challenging to precisely reconstruct the physico-chemical, petrological and structural parameters which  
243 control rheology as a function of depth during eruption. For the late-stage spine, Nakada and Motomura  
244 (1999) proposed that it formed due to a lower effusion rate, which resulted in extensive magma  
245 degassing and crystallisation, and thus high viscosity, which promoted rupture and exogenic growth at  
246 relatively low strain rates (e.g., Hale and Wadge, 2008; Goto, 1999). Extrusion occurred through  
247 pulsatory magma ascent, accompanied by ~40 h inflation/deflation cycles (Yamashina et al., 1999) and  
248 a rhythmic pattern of summit earthquakes, interpreted to result from magma rupture in the top 0.5  
249 kilometre of the conduit (Lamb et al., 2015; Umakoshi et al., 2008); waveform correlation of the seismic  
250 record revealed rhythmic seismicity grouped into two primary clusters (Lamb et al., 2015). Hornby et  
251 al. (2015) statistically analysed the slip duration of seismic events in the clusters, defining a mode and  
252 mean of 0.1 s. As magma ascent occurred through an inclined conduit (Umakoshi et al., 2008), the spine  
253 extruded at an inclined angle of ~45° towards the ESE (Fig. 2a) and increasingly leaned against the  
254 lower fault zone as extrusion rate waned, causing the shallowing of seismogenic magma rupture in this  
255 area (Lamb et al., 2015). In contrast, the upper fault zones may have opened up as the spine settled, thus  
256 triggering rupture at increasing depth and promoting preferential pathways for fluid flow (Lamb et al.,  
257 2015). By the end of the eruption, the spine achieved approximate dimensions of 150 m length, 30 m  
258 width and 60 m in height (Nakada and Motomura, 1999; Nakada et al., 1999); it is complemented by  
259 multiple fragments of spines, extruded earlier in the eruptive phase, which we examine in this study.  
260 Unfortunately, the lower and upper fault zones are not observable in the spine exposures, but the  
261 northern lateral conduit margin contains well-defined shear zones (Smith, 2002; Smith et al., 2001),  
262 which are revisited here and augmented by structural and microtextural descriptions as well as porosity  
263 and permeability constraints. Our study of the spine sheds new light on the permeability evolution of  
264 its shear zones, and thus the nature of outgassing during the waning phase of the 1990-1995 eruption.

265

## 266 2. Materials and Methods

### 267 2.1 Localities and sample collection

268 The 1994-95 lava spine was investigated during two field campaigns, in November 2013 and  
269 May 2016. Close structural examination at different scales forms the basis of this study along with  
270 porosity and permeability measurements, using field and laboratory equipment. Owing to the inclination  
271 of the spine (extruded towards the east), large blocks ranging from 5 to 20 m-wide are dislocated from  
272 the front of the *in situ* western main spine structure (Fig. 2a, b). Here, we investigated two blocks that  
273 reveal a central shear zone (CSZ) and marginal shear zone (MSZ) that developed in the spine. These  
274 detached, yet fully intact, spine blocks were selected owing to their contrasting shear textures that would  
275 have represented different positions within the volcanic conduit during magma ascent and extrusion  
276 (i.e., central vs. marginal), thus allowing assessment of syn-eruptive outgassing pathways. The marginal  
277 shear zone (MSZ) block, located ~60 m east of the main spine (Latitude: 32.76131° Longitude:  
278 130.29983°), was carefully sampled to quantify the spatial distribution of permeability across the spine  
279 margin (samples A-H; Fig. 2c). The CSZ block, located centrally between the main spine and MSZ  
280 (Latitude: 32.761271° Longitude: 130.299472), features the dilatational cavity (described in Smith et  
281 al., 2001) and was also studied *in situ*, using non-destructive methods to preserve the integrity of this  
282 exemplary feature. The main spine and CSZ are protected by UNESCO heritage site regulations (Figs.  
283 1c, 2a), thus only permitting *in situ* sample collection from the MSZ.

284

## 285 2.2 Sample preparation

286 Samples collected from the marginal shear zone were cut and cored parallel to the shear  
287 direction and perpendicular to the shear plane in order to constrain the anisotropy developed in shear  
288 zones. A total of eight thin sections (fluorescent dyed) were prepared for microtextural analysis (labelled  
289 A-H). For the largest samples (A, B, C, E, H; see Fig. 2c-d) a set of 2-3 cylindrical cores (two parallel  
290 and one perpendicular to shear plane) were prepared with a diameter of 26 mm and a length of 30 or 13  
291 mm, depending on the size of the sample. Within the highly sheared sample B (Fig. 2c-d), which is  
292 directly adjacent to the fault and gouge zone, multiple sets of cores of 20 mm diameter were prepared,  
293 closely spaced, to obtain porosity/permeability determinations at a higher resolution across this defining  
294 part of the shear zone.

## 295 2.3 Microstructural analysis in 2D and 3D

296 2D analysis of the microstructures exhibited across the shear zones was carried out using a  
297 Leica DM2500P optical microscope in plane polarised and ultraviolet (UV) light, as well as a Philips  
298 XL30 scanning electron microscope (SEM) in backscattered electron (BSE) mode, set at 20 kV and 10  
299 mm working distance. For this purpose, representative features were imaged for each sample across the  
300 shear zone (Fig. 3).

301 To further evaluate the architecture of the porous network in three dimensions (3D), four  
302 samples collected across the shear zone were scanned using a phoenix nanoton® m x-ray computed  
303 tomography scanner to produce high-resolution reconstructions with a voxel size of 11.111  $\mu\text{m}$ . For  
304 each sample we acquired 1440 radiographs, scanning 360°, under the following conditions: exposure  
305 time of 1000 ms; voltage of 80 kV; current of 120  $\mu\text{A}$ ; 0.2 mm aluminium filter. The radiographs were  
306 then reconstructed using the inverse Radon transformation (Radon, 1986), resulting in a 3D image of  
307 the sample. These files were processed in FEI Avizo and ImageJ/Fiji software to illuminate the  
308 permeable, porous network.

309

## 310 2.4 Porosity measurement in the laboratory

311 Each core was dried in an oven at 50 °C overnight, then kept in a desiccator (for thermal  
 312 equilibration to ambient conditions) before being weighed and loaded in a pycnometer. The fraction of  
 313 connected pores (which controls permeability; Colombier et al., 2017) was determined using a  
 314 Micromeritics AccuPyc II 1340 helium pycnometer. The porosity determination first necessitated  
 315 measurement of the geometric volume of the sample ( $V_{sample}$ ). Then, once inserted in the specimen  
 316 chamber of the pycnometer, helium gas was injected in the chamber to estimate the volume taken up  
 317 by the solid fraction of the sample, thus providing the skeletal volume ( $V_{skeletal}$ ) of the rock. The  
 318 fraction of connected pores ( $\phi_{connected}$ ) in a sample was then calculated via:

$$319 \quad \phi_{connected} = \frac{(V_{sample} - V_{skeletal})}{V_{sample}} \quad (1).$$

320

### 321 2.5. Permeability determination in the laboratory

322 The prepared cores were jacketed with a Viton™ tube and inserted in a hydrostatic cell from  
 323 Sanchez technologies to measure permeability and pore volume as a function of pressure. The jacketed  
 324 samples were externally loaded using a Maximator® oil pump to various confining pressures ( $P_c$ ) and  
 325 internally loaded using distilled water to an average pore pressure ( $P_p$ ) of 1.25 MPa, in order to obtain  
 326 a range of effective pressures ( $P_{eff} = P_c - P_p$ ) from 5 to 100 MPa. Each time the sample was loaded to a  
 327 new confining pressure increment, the volume of water expelled from the void space in a given sample  
 328 (due to compaction) was monitored to constrain pore volume change due to crack closure as a function  
 329 of pressure (Lamur et al., 2017); this allowed us to monitor when the samples (i.e., their microstructure)  
 330 had equilibrated to the set conditions at each pressure step. Steady-state flow permeability ( $k$ ) was then  
 331 measured by applying low pore pressure gradients ( $\Delta P$ ) of 0.5 and 1.5 MPa to ensure laminar flow with  
 332 no slip conditions (after Heap et al., 2017a) to satisfy Darcy's Law:

$$333 \quad k = \frac{Q\eta L}{A(\Delta P)} \quad (2),$$

334 where  $Q$  is the flow rate monitored through the sample ( $\text{m}^3\text{s}^{-1}$ ),  $\eta$  is the viscosity of the water in pores  
 335 (Pas),  $L$  is the length of the sample (m), and  $A$  is the cross-sectional area of the sample ( $\text{m}^2$ ).

336

### 337 2.6 In-situ permeability measurements in the field

338 To measure the permeability of rocks in the central shear zone (CSZ; Fig. 1c) that could not be  
 339 sampled for laboratory testing due to preservation restrictions, we used a non-destructive, portable, air  
 340 permeameter (TinyPerm II) from New England Research, which estimates permeability by monitoring  
 341 pressure recovery rate from a vacuum, based on the concept of transient pulse permeability (Brace et  
 342 al., 1968). The apparatus is hand-held and needs to be employed carefully to maintain a consistent seal  
 343 between the nozzle of the permeameter and rock surface throughout the measurements (lasting up to a  
 344 few tens of minutes). It may be used to determine the permeability of rocks between approximately  $10^{-12}$   
 345 to  $10^{-16} \text{ m}^2$  (Farquharson et al., 2015; Kendrick et al., 2016; Lamur et al., 2017). In this study, three  
 346 transects were measured across the central shear zone and all measurements were performed twice to  
 347 ensure precision of the method (as determined in Lamur et al., 2017).

348

## 349 3. Observations and results

350 The 1994-95 spine structure at Mount Unzen is exposed in several large, segmented blocks  
351 (Fig. 1c-d; Fig. 2a-b). A thorough structural description of the main spine structure and subsidiary block  
352 (e.g., CSZ) can be found in Smith et al. (2001); here we highlight the main features. The lava spine is  
353 split into a few very large, primary blocks, ~20-30 m wide and high (Fig. 1c-d, 2a-b), broken roughly  
354 perpendicular to extrusion direction: westward and inclined (see Fig. 2b). The CSZ block seen in Figure  
355 1c shows a >8-m wide variably deformed core (I) lying adjacent to a 2-m wide intensely sheared zone  
356 (II), bordered to the north by a dextral fault and coupled to a large, indurated breccia (III), uplifted from  
357 the surrounding dome. The lower and southern edges were not exposed. The upper edge of the spine  
358 was not accessible, but we noted large, incoherent brecciated blocks. The rear of this outcrop as well as  
359 the main *in situ* spine structure exhibit irregular, metre-scale polygonal joints, although these are not  
360 developed in the face of the outcrop studied here (Fig. 1c). Additional fragments of the spine occur in  
361 a few subsidiary blocks (e.g. Fig. 1d), located a few tens of meters to the east of the main spine (Fig.  
362 2a). These blocks, which were emplaced prior to the main spine, expose several sections through the  
363 spine, and reveal the evolving architecture of the shear zone in the shallow magmatic conduit. One such  
364 block, shown in Figure 1d, exhibits a ~1-m wide shear zone, bordered to the left by a set of oblique  
365 tensile fractures, reaching 2-5 m in length and spaced at ~3 to ~10 cm intervals, and to the right by an  
366 indurated breccia. This prominent block was not sampled or further studied to preserve its integrity.

367

### 368 3.1 *The marginal shear zone*

#### 369 3.1.1. *Structural and microtextural observations*

370 Our primary field location for this study was a 4.7-m wide block of the spine, exposing the  
371 northern marginal shear zone consisting of gouge, sheared lava and the spine core (Fig. 2c-d). The  
372 outcrop displayed mild surface weathering, in the form of a thin (micron-size) veneer of unknown  
373 precipitate on the rock surface (which was inclined at an angle of ca. 40° towards the West). This thin  
374 veneer did not visually obstruct any primary magmatic textures and structures, and the shear texture  
375 was clearly visible, yet we it would prevent accurate field permeability constraints. Four distinct degrees  
376 of shear were visually defined through textural examination and changes in surface roughness across  
377 this section of the conduit (Fig. 2c-d): a fault gouge zone (sample A) bordering a high-shear zone  
378 (samples B, C, D), a moderate-shear zone (samples E, F) and low-shear spine core (samples G, H) in  
379 decreasing order of surface roughness and visually observable fracture density variations; quantitation  
380 of fracture density was not attempted as we deemed the thin veneer may have prevented meaningful  
381 accuracy. This shear-based division is consistent with a complementary investigation of the  
382 mineralogical characteristics of this shear zone (Wallace et al., 2019). The contacts between shear zones  
383 trend approximately E-W in the outcrop (Fig. 2c,d), and so roughly parallel to the spine emplacement  
384 direction to the ENE, despite the detachment of this spine block from the main intact spine body to the  
385 west. Eight samples were systematically collected across this shear zone for further analysis (labelled  
386 A-G in Fig. 2c,d): eight for 2D microstructural analysis (PPL, UV light and BSE imagery; Fig. 3), four  
387 for tomographic imaging (Fig. 4) and five for porosity and permeability determination (Fig. 5-6). [Note  
388 that multiple cores were obtained from the five blocks sampled for laboratory measurements.]

389 The spine core, termed low shear herein (~1.5 m wide; Fig. 2c, d), exhibited a smooth surface  
390 and the phenocrysts showed no preferred orientation at the macroscopic scale. In samples G and H  
391 collected from the low shear zone (Fig. 3), phenocrysts of plagioclase, amphibole, biotite (plus minor  
392 quartz) are typically euhedral, largely intact and up to ~5mm in length (Fig. 3); groundmass microlites  
393 also show no preferred orientation in BSE images. The porous structure is characterised by a diktytaxitic  
394 texture, composed of some large, irregular, vesicles with ‘ragged’ edges, appearing intrinsically related

395 to the presence of surrounding phenocrysts (single white arrows on UV light images in Fig. 3). Small  
396 fractures are often seen to originate from these large vesicles, penetrating pervasively through both  
397 phenocrysts and the groundmass (double white arrows in Fig. 3). The groundmass contains abundant  
398 small vesicles, showing a high degree of connectivity as revealed by tomography (Fig. 4g-h).

399 The moderate shear zone is approximately 2 m wide (Fig. 2c, d). In this zone, we observed an  
400 increased fracturing of phenocrysts and changes in the distribution of porosity. Scrutinising the sample  
401 E via microscopy, we observe that the phenocrysts, which rarely exceed 2 mm in size in this zone, are  
402 commonly micro-fractured (Fig. 3). The vesicles are occasionally large ( $\lesssim 3$  mm) and connected (Fig  
403 3, 4e-f), and while the vesicular texture remains diktytaxitic (as in the low shear spine core), the vesicles  
404 in sample E appears increasingly aligned and localised around phenocrysts as the magnitude of shear  
405 increases towards the fault; similarly, the microlites show increasing degrees of alignment (revealed by  
406 undulose extinction angles; see Wallace et al., 2019). Thin bands ( $<200$   $\mu\text{m}$  width) of reduced porosity  
407 are observed to localise in the groundmass (see facing double arrows in UV light images in Fig. 3),  
408 which are notably absent in the low shear zone; these are (sub-)parallel to the shear plane. The  
409 tomographic reconstructions show irregular vesicles, which are surrounded by fractures and invaded by  
410 rock fragments (Fig. 4e). These vesicles enhance the connectivity of the porous network (Fig. 4f).

411 The high shear zone is approximately 1 m wide (Fig. 2c, d) and marks the beginning of micro-  
412 and meso-scopic shear bands, at a scale of the order of a few millimetres, near-parallel with the direction  
413 of shear; these increase in abundance and scale nearer the fault, especially within the final 0.1-0.2 m  
414 (see features denoted in Fig. 2c-d as well as enlarged in the inset). The bands, which form a pervasive  
415 foliation (S), consist of elongate, white porphyritic plagioclase lenses, fractured and crenulated. The C-  
416 S fabrics are parallel in this area. These porphyritic bands are flanked by reddish-brown groundmass as  
417 well as thin, elongate biotite phenocrysts (see sample B “fresh surface” in Fig. 3). The plagioclase and  
418 biotite commonly exhibit a mineral fish texture. Under the microscope, we observe that the biotite show  
419 undulose extinction from crystal-plastic deformation (see Wallace et al., 2019, for a detailed crystal  
420 plasticity study). Intense banding (observed as faint lineations of reduced porosity under UV light in  
421 the moderate shear zone; Fig. 3) is observed adjacent to, and running parallel with, the fault-gouge  
422 contact. The bands are up to  $\sim 1$  mm wide and display variations in porosity under UV light (Fig. 3), as  
423 also revealed by tomography (Fig. 4c-d). The dense bands are traversed by hairline fractures a few  
424 hundred microns in length and contain a few isolated vesicles ( $\lesssim 70$   $\mu\text{m}$ ), generally adjacent to large  
425 phenocryst fragments (samples B and C in Fig. 3). More porous bands display disordered and  
426 fragmental textures (sample B), with abundant, irregular large pores and cracks, and pulverised  
427 phenocrysts (PPL and UV light in Fig. 3); macroscopically, the most porous bands often appear like  
428 ragged tensile fractures. The transition between dense and porous bands is abrupt, occurring over a few  
429 tens of microns (BSE images of samples B and C in Fig. 3). Microlites and microphenocrysts are aligned  
430 with the banding, and thus with shear and extrusion direction (Fig. 3). The high shear region of the  
431 spine is further crosscut by multiple sub-parallel curvilinear extensional bands (i.e., weakly defined  
432 fractures), up to  $\sim 1$  m in length, and trending  $\sim 57^\circ$  from the primary C-S fabrics in a Riedel-like fashion  
433 (Fig. 2c, d); some of these bands extend into the moderate shear zone but only faintly. These bands,  
434 spaced by 3-6 cm ( $\sim 4.5$  cm in average), show opening of ca. 1-2 mm in places. [Note that the blue traces  
435 in Figure 2 denote the general attitude, not the spacing, of the bands]. The Riedel fractures appear to be  
436 associated with a set of faint, conjugate fractures (R'), although their observation is not ubiquitous  
437 across the high-shear zone.

438 The fault zone hosts up to ca. 0.2-m thick gouge material (Fig. 2c,d). The contact between the  
439 gouge and the high shear zone is generally sharp, and often planar, although we observed small  
440 embayments, especially along C-S fabrics in the neighbouring high shear zone (Fig. 2d). [Note that the

441 extent of the gouge is not exposed equally across the outcrop as material was likely lost during  
442 separation of this block from the main spine upon eruption; so the surface does not reflect the contact  
443 geometry. This material loss also led to obliteration of vestiges of a pseudotachylyte, suggested by local  
444 partial melting textures presented by Wallace et al. (2019)]. The gouge is typified by well-consolidated,  
445 fine-grained cataclasite with some larger rounded clasts up to ~15 mm in diameter (sample A; Fig. 2c  
446 inset). The gouge is matrix supported and displays a strong foliation parallel to spine extrusion direction.  
447 Conjugate fractures form a dominant feature contributing to the porosity of the gouge. Microscopically,  
448 the rock is pervasively fragmented (sample A in Fig. 3); the few phenocrysts that remain relatively  
449 intact often display signs of deformation. The fragments in the gouge are generally densely compacted  
450 and the porosity is uniformly distributed, with little banding or preferred orientation of fragments at the  
451 microscopic scale, although connected pores occasionally exhibit a degree of alignment at small scale  
452 (Fig. 3) and at large scale as observed via x-ray tomography (Fig. 4a-b).

453

### 454 3.1.2 *Connected porosity across the marginal shear zone*

455 The porosity of the rocks, determined via pycnometry, indicates variations between 8 % and 27  
456 % across the shear zone and in the fault gouge; Figure 5a displays the average of multiple measurements  
457 from the different cores prepared from each sample. The measurements indicate that the high shear zone  
458 generally holds slightly lower porosities than surrounding areas. Within the high-shear zone (sample B)  
459 we measured significant variations in porosity ranging between 8 % and 15 % (at ambient conditions)  
460 due to flow bands (e.g., in sample B); yet, the coarseness of samples measured prevent accurate  
461 quantification of the highly spatially variable porosities observed in hand specimen.

462 When loading the samples (cored parallel with to spine extrusion direction) in the hydrostatic  
463 pressure vessel, we observed a nonlinear decrease in porosity of up to 4 % by increasing the effective  
464 pressure to 100 MPa (Fig. 5b). The data shows a similar dependence of porosity on effective pressure  
465 for the coherent samples from the low, moderate and (densest part of) high shear areas, with a slightly  
466 larger reduction in porosity with effective pressure in the initially most porous, high shear bands and  
467 granular gouge sample (Fig. 5b).

468

### 469 3.1.3 *Permeability across the marginal shear zone*

470 The permeability of the rocks collected across the spine segment reveals a ~1-m wide region of  
471 low permeability in the high shear zone, compared with the moderate shear zone, the low shear spine  
472 core and fault gouge (Figs. 5, 6). There appear to be abrupt variations in permeability (decrease and  
473 increase) in sheared rocks directly adjacent to the fault gouge, due to the alternation between dense and  
474 porous shear bands.

475 The data show considerable differences in the permeability parallel and perpendicular to the  
476 plane of shear (Fig. 3c,d) across the shear zone (Fig 6a,b). In the high shear zone permeability was  
477 found to be higher in the plane of shear (*i.e.*, parallel with extrusion direction) than perpendicular to it,  
478 whereas in the moderate and low shear zones, as well as in the gouge, permeability was essentially  
479 isotropic. Anisotropy is cast here as a ratio between the permeability parallel and perpendicular to the  
480 shear plane (Fig. 6c). The anisotropy is most pronounced in the high shear zones, where, in one instance,  
481 the permeability ratio increases dramatically from three to over seven times larger parallel than  
482 perpendicular to the shear plane with increasing confining pressure in a hydrostatic pressure vessel (Fig.  
483 6c). In other samples, the anisotropy increase with pressure is less or even negligible, indicating the

484 heterogenous nature of the high shear zone. This sensitivity to confinement is due to the presence of the  
485 distinct dense and porous bands in the sheared lava (Fig. 5b, 6); in the cores parallel to the shear plane,  
486 fluid can flow through porous bands from top to bottom of the sample, whereas perpendicular to shear,  
487 fluids must pass through both dense and porous bands to traverse the sample. Fluid flow in the  
488 denser areas will be dominated by channelling through narrow fractures (sub-horizontal in BSE images  
489 in samples B and C in Fig. 3), which are more susceptible to closure by increasing effective pressure  
490 than equant pores (e.g., Kendrick et al., 2021). Although this process occurs during confinement in both  
491 orientations, it only impacts permeability perpendicular to shear direction, and so contributes to  
492 enhanced anisotropy of permeability in banded shear fabrics under confinement (Kendrick et al., 2021).

### 493 3.2 *Central shear zone*

#### 494 3.2.1 *Structural observations*

495 The second feature of interest is the cavity exposed in the central shear zone block (Fig. 1c and  
496 2a). This section of the spine has been described in detail by Smith et al. (2001); here, we review key  
497 aspects observed in the field as no samples were collected to conserve the exposure of this world-class  
498 feature. We only examined the rocks forming this structure and performed non-destructive, *in-situ*  
499 testing.

500 The central shear zone (CSZ) is located near the centre of the spine core (Fig. 1c). Its primary  
501 feature is the presence of a porous cavity, which curves and pinches out (upward) from the end of a  
502 dominant, 9-cm wide fracture, extending approximately 3 m in length (determined from the visible  
503 extent of the exposure). Unlike the aforementioned marginal shear zone, which displays an increased  
504 degree of shear towards the spine margin, the central shear zone exhibits an increase in shear towards  
505 the centre of the spine. From left to right (i.e., northward) on Figure 7, we note an increase in aligned,  
506 bent and broken phenocrysts as well as aligned shear bands (ostensibly parallel with the dominant  
507 fracture), fractures and surface roughness, which terminates upon intersecting the end cavity; beyond  
508 which point, the rocks show no clear evidence of shear, including shear bands, elongate pores or aligned  
509 crystals. This is evident in the field photograph (Fig. 7) as steeply inclined porous bands which end  
510 against the southern (i.e., right) side of the cavity; on the southern side the sheared lava exhibits a higher  
511 porosity than the surrounding undeformed rocks (although this could not be quantified in the field).  
512 Approximately 1 m above the pinched-out tip of the main cavity, we observe the presence of a  
513 secondary porous cavity (Fig. 1c inset), approximately 60 cm long, and elongated parallel to the fracture  
514 that connects to the main cavity.

515

#### 516 3.2.2 *Permeability across the central shear zone*

517 The permeability of the rocks in the central shear zone was measured along three transects in  
518 two field campaigns (in November 2013 and May 2016) to negate potential influence from variable  
519 degrees of water saturation of the rocks at different times of year. Our field measurements are consistent  
520 with one another. The permeability varies very little in the undeformed areas of the outcrop (i.e., on the  
521 right-hand side of the fracture in Fig. 7) for all transects, with an abrupt increase in permeability up to  
522 three orders of magnitude in the 9cm wide central cavity, and elevated permeability in the ~40 cm wide  
523 proximal sheared area to the left of the fracture.

524

## 525 4. **Interpretation**



526 The contrasting permeability, porosity and (micro)structural changes observed across the  
527 marginal and central shear zones reveal the impact of shear and distinct modes of magma deformation  
528 during shallow conduit ascent. Here we interpret each of these key features for the development of  
529 volcanism at lava domes.

### 530 *Marginal shear zone*

531 The marginal shear zone is characterised by a 3-m wide zone in which strain caused changes in  
532 the porous structure, via crushing of the pore walls as well as distortion and failure of the crystalline  
533 phase; these promoted an increased reduction in pore volume and permeability towards the fault,  
534 especially in the high shear zone. Smith et al. (2001) invoked the effects of gravitational forces during  
535 post-emplacment flow of the lobes as a mechanism for the development of ‘ragged’ pores and  
536 porous/dense flow banding in dome lavas at Unzen volcano. Yet, such diktytaxitic structures have been  
537 observed in small surficial dome blocks at Santiaguito volcano (Guatemala), which have not suffered  
538 from gravitational effects associated with flow along the flanks (Rhodes et al., 2018); they have also  
539 been observed at Merapi volcano, where they were attributed to late-stage gas filter pressing of a silica-  
540 rich melt phase (Kushnir et al., 2016). The commonality between these observations is that they occur  
541 in crystal-rich magmas, where crystals hamper the presence and distribution of exsolved fluids and  
542 interstitial melt, leading to ragged pore boundaries with protruding crystals. At Unzen, the character  
543 and distribution of the porous network rather evidence the importance of deformation which was  
544 pervasive and commonly compactant in the marginal high shear zone. Experiments have shown that in  
545 the ductile field, material may deform by sustaining substantial compaction without the propensity for  
546 developing localised strain (Rutter, 1986) – a regime that generally results in a permeability reduction  
547 through shear (Ashwell et al., 2015; Kushnir et al., 2017b; Heap et al., 2015a; Heap et al., 2015b). In  
548 this regime, magma deformation may result in crystal-plastic distortion and failure (Kendrick et al.,  
549 2016), as witnessed at Unzen (Wallace et al., 2019). Thus, we interpret the bulk of the marginal shear  
550 zone as the result of ductile deformation, which resulted in distributed, pervasive shear over a width of  
551 3 m. Within this part of the conduit, the high shear zone displayed the highest degree of shear-enhanced  
552 compaction.

553 However, ductility alone is insufficient to describe the marginal shear zone. For instance, the high-shear  
554 area exhibits a foliation (S plane) and fractures (C plane) parallel to the shear plane, which is then  
555 crosscut (parallel but undulating) by a marginal fault hosting gouge formed by comminution and  
556 cataclasis, containing conjugate fractures. The composite C-S fabric in the high shear zone is  
557 increasingly penetrative towards the fault core (at the gouge contact), and its parallel C and S planes  
558 indicates that the shear zone accommodated significant strain. This is supported by observation that  
559 curvilinear Riedel fractures have developed and overprinted the C-S fabric at an angle of 57° (cf.  
560 Ramsay, 1980). Such an angle is consistent with a lava body undergoing rupture following sustained  
561 ductile deformation (e.g., Lavallée et al., 2013); it is also consistent with the progressive thickening of  
562 a shear zone formed via simple shear with a small component (<10 %) of pure shear (assuming pure  
563 and simple shear are planar; Fossen and Cavalcante, 2017); this minor pure shear component is further  
564 supported by the presence of weakly defined conjugate fractures crosscutting the Riedel fractures. Both  
565 the gouge and the fractures through the high shear zone were constrained to have locally higher  
566 permeability and porosity than the bulk of the shear zones: features characteristic of dilational  
567 deformation resulting from macroscopically brittle failure (Heap et al., 2015a; Heap et al., 2015b;  
568 Laumonier et al., 2011). Riedel fractures generated in experimentally deformed magma have been  
569 described as important pathways to redistribute fluids across shear zones (Laumonier et al., 2011), and  
570 we anticipate the impact would be similar at Unzen; the Riedel fractures in the marginal shear zone only  
571 reached ~1m in length, but the marginal shear zone in other blocks (Fig. 1d) contain oblique Riedel  
572 fractures that reach 2-5 m in length (Fig. 1d) which would have formed efficient fluid flow pathways.

573 Thus, we interpret the marginal shear zones to reflect the evolution of magma shearing across the ductile  
574 to brittle transition during shallowing of the magma plug, which impacted fluid flow during the spine  
575 eruption.

#### 576 *Central shear zone*

577 The central shear zone detailed in this study has a very different character. Macroscopic  
578 observations of numerous cracks suggest that it is dominantly dilational, as supported by the drastic  
579 increase in permeability towards the fault and cavity. Despite having opened by ~9 cm, the main fracture  
580 tip is blunted as it terminates in a curvilinear cavity, and seemingly disappears before reappearing as a  
581 secondary cavity 1 m above (Fig. 1c inset). This is akin to areas of reduced density that develop ahead  
582 of a crack tips during material failure in the lab (e.g., Célarié et al., 2003) and indicates immature shear  
583 that was insufficient to enable the continuous propagation of a fault across the whole spine. This, in  
584 conjunction with the observation that shear becomes more pronounced towards the centre of the spine,  
585 suggests that the areas undergoing shear may have locally shifted towards the conduit core; yet,  
586 displacement was not extensive. The reason for this shift is difficult to assert, but we posit that the  
587 shallow calving of blocks from the spine front, progressive inward cooling and/ or the higher porosity  
588 of the magmas in the conduit core (compared to a denser, compacted and strained conduit margin) may  
589 have shifted the locus of deformation towards the conduit core at the end of the eruption.

590 The shear zones studied here indicate that the dominant deformation regime of magma may  
591 evolve spatially and temporally during ascent in volcanic conduits, which would modify the magma's  
592 permeability and its ability to localise and channel outgassing during the effusion of lava domes.

593

## 594 **5. Discussion**

### 595 *Permeability in volcanic environments*

596 The power of volcanic eruption models relies on an understanding of the coupling between  
597 magma and volatiles in volcanic conduits (Sparks, 1997), yet a description of dynamic permeability of  
598 deforming magma eludes us. The studies of eruptive products have provided first order constraints on  
599 the relationship between permeability and porosity (Fig. 8; Klug and Cashman, 1996; Mueller et al.,  
600 2005; Farquharson et al., 2015) for various types of volcanic rocks (e.g. explosive clasts vs effusive  
601 lavas), including the presence of heterogeneous structures (Farquharson et al., 2016c; Kolzenburg et al.,  
602 2012; Lamur et al., 2017; Kendrick et al., 2021), and these constraints have been invoked in diverse  
603 models to assess how magma permeability may evolve leading to eruption (Burgisser et al., 2019;  
604 Edmonds et al., 2003). However, the deformability of magma imposes constant changes to the porous  
605 permeable network and to date, only a few studies have measured or assessed the transience of  
606 permeability and porosity during magma deformation (Okumura et al., 2010, 2012; Kendrick et al.,  
607 2013; Ashwell et al., 2015; Kennedy et al., 2016), especially *in operando* (Wadsworth et al., 2017;  
608 Wadsworth et al., 2021; Kushnir et al., 2017a; Heap et al., 2017b). Considering the range of pressure  
609 conditions (e.g., pore pressure gradient, local deviatoric stress) and magma properties, none of these  
610 studies has yet succeeded in fully reconstructing the evolution of porosity and permeability of magma  
611 shearing during ascent in volcanic conduits.

612 The rocks sampled across the shear zone and in the fault gouge at Mount Unzen vary in porosity  
613 between 8 % and 27 %; this range is slightly narrower than the porosity range (4-48 %) covered by  
614 blocks shed by pyroclastic density currents originating from the domes during the 5-year eruption (see  
615 Fig. 8; Kueppers et al., 2005; Coats et al., 2018; Kendrick et al., 2021; Scheu et al., 2007; Mueller et

616 al., 2005). The narrower range exhibited by the spine shear zones may reflect the occurrence of fewer  
617 porosity-modifying mechanisms (e.g., post-fragmentation vesiculation) in the highly viscous spine lava  
618 compared to those which occurred throughout the entire course of the eruption, which are represented  
619 by the blocks at the foot of the volcano. We see the largest contrast when we compare the permeability  
620 range of the lavas which erupted through the spine at the end of the eruption ( $\sim 10^{-15}$  to  $\sim 10^{-14}$  m<sup>2</sup>, at the  
621 lowest effective pressure) with that obtained from rocks recovered by drilling through the eruptive  
622 conduit at a depth of  $\sim 1.5$  km ( $\sim 10^{-17}$  to  $\sim 10^{-19}$  m<sup>2</sup>) in the framework of the Unzen Scientific Drilling  
623 Project, drill hole 4 (USD4) (Watanabe et al., 2008). The latter rocks, originating from magma stalling  
624 at depth, reflect greater time under compactant conditions and porosity infill and reduction from  
625 secondary mineral precipitation (Yilmaz et al., 2021). The large difference in permeability between the  
626 two datasets alludes to the highly variable spatial and temporal variation of magma permeability within  
627 even a single volcanic system.

628 Previous investigations of permeability in shallow volcanic conduits have highlighted the  
629 existence of dilational shear zones, whereby the conduit margin is bound by a permeable ‘damage halo’;  
630 this has been proposed through both field (Saubin et al., 2019; Pallister et al., 2013a; Gaunt et al., 2014;  
631 Wallace et al., 2019; Ryan et al., 2020; Sparks et al., 2000; Watts et al., 2002; Holland et al., 2011) and  
632 laboratory (Lavallée et al., 2013; Laumonier et al., 2011) studies. These constraints indicate a dilation  
633 zone, with permeability higher by up to 1.5 orders of magnitude and variable degrees of anisotropic  
634 shear fabrics, causing preferential channelling of fluids in the direction of extrusion (Wright et al., 2006;  
635 Gaunt et al., 2014; Wallace et al., 2019; Ryan et al., 2020). Pore space connectivity is enhanced by  
636 fracturing (Lamur et al., 2017; Tiab and Donaldson, 2016), which would contribute to the development  
637 of anisotropy and would preferentially channel fluids along the conduit margin, promoting concentric  
638 or ring-like gas emissions, as for instance exemplified at Santiaguito, Guatemala (Lavallée et al., 2013;  
639 Holland et al., 2011). Connectivity may however be lost at the expense of fracture healing (Lamur et  
640 al., 2019) or sintering (Ryan et al., 2020; Wadsworth et al., 2016). Here, at the conduit centre at Unzen,  
641 we observed a localised dilational shear zone up to three orders of magnitude more permeable than the  
642 surrounding magma; thus, the scale of dilation exceed that observed in marginal shear zones at Mt. St-  
643 Helens (Gaunt et al., 2014) and at Chaos Crags (Ryan et al., 2020). This zone spans a relatively narrow  
644 section of the conduit and appears to be a late, immature feature that is possibly related to shear during  
645 the final stages of ascent of the magma plug and/ or structural readjustment during failure and calving  
646 of portions of the spine to the ENE. Instead, the primary (and volumetrically most significant) marginal  
647 shear zone studied at Unzen is mostly compactional and exhibits a lower permeability than the  
648 surrounding magma, particularly in the plane perpendicular to shear direction. Compaction may have  
649 been favoured in the marginal shear zone at Unzen, compared to dilation at Mt St-Helens and Chaos  
650 Crags due to the relatively higher porosity of the ascending magma [20% at Unzen, vs 10% and 12-  
651 15% at Mt. St-Helens (Gaunt et al., 2014) and Chaos Crags (Ryan et al., 2020) respectively]; it may  
652 also reflect lower viscosities, and/ or deformation at greater effective mean stress in the system or at  
653 relatively lower strain rates (Figure 9). Indeed, the marginal shear zone is overprinted by faulting, which  
654 suggests that compaction took place at greater depth and/ or during inter-seismic periods of slower  
655 ascent. Seismic analysis indicated that seismogenic faulting was episodic and shallow, likely originating  
656 in the upper 500 m of the conduit (Umakoshi et al., 2008; Lamb et al., 2015); so, whilst below this depth  
657 shear may have prompted compaction, above this depth pulsatory magma shearing may have resulted  
658 in switches between compactional and dilatant shear, causing locally higher permeability fractures  
659 through the sheared magma, and a permeable marginal fault gouge by cataclasis (Fig. 9). Such  
660 intermittent seismic stressing may also serve to weaken surrounding country rocks and modify  
661 permeable pathways (Schaefer et al., 2020).

662

664 The presence and overprinting of compactional and dilational shearing modes in close  
665 proximity in a given magmatic extrusion demands appraisal. The ductile-brittle transition of materials  
666 has long been studied and is generally better understood for rocks than magmas as more low-  
667 temperature tests have been carried out (Paterson and Wong, 2005; Rutter, 1986; Heap et al., 2015a).  
668 Reconstruction of yield caps (or curves), based on the shear stress required for rupture or flow of  
669 materials at different effective mean stress, have shown that porous rocks undergo a transition from  
670 macroscopically brittle to ductile deformation modes with increasing effective pressure (Fig. 9b); this  
671 transition sets in at lower effective pressure (i.e., either at shallower depths or with higher pore  
672 pressures) if the material is more porous (Heap et al., 2015a). However, magma is viscoelastic, thus  
673 depending on the timescale of observations magma may behave as a solid; in essence, as a rock.  
674 Magmas abide to the glass transition so that at long observation timescales or under slow deformation,  
675 they flow; but at short timescales or if strain rate is high, they may rupture (Dingwell, 1996). The strain  
676 rate to meet this transition decreases if melt viscosity increases due to cooling, crystallisation,  
677 degassing, and/ or vesiculation (Wadsworth et al., 2018; Dingwell and Webb, 1989, 1990; Cordonnier  
678 et al., 2012; Cordonnier et al., 2009; Coats et al., 2018; Lavallée et al., 2013; Lavallée et al., 2008). The  
679 glass transition of silicate melts, which controls the deformation mechanisms of magmas (viscous or  
680 brittle), thus impacts their deformation modes, brittle or ductile (be it viscous flow or cataclastic flow);  
681 applicability of the concept of yield caps to volcanic rocks and magma, as shown in Figure 9b, have  
682 been reviewed by Lavallée and Kendrick (2020). In a scenario where magma ascends, deforms and  
683 outgasses during an eruption, such as during spine extrusion at Unzen, magma may undergo a transition  
684 from a macroscopically ductile to brittle deformation mode due to a reduction in effective pressure  
685 (from ascent or due to pore pressure increase; Heap et al., 2017b), densification (Heap et al., 2015a;  
686 Coats et al., 2018), viscosity increase (cf. Dingwell and Webb 1990) or if the strain rate locally increases  
687 (Coats et al., 2018; Lavallée et al., 2013; Lavallée et al., 2008).

688 Nakada and Motomura (1999) proposed that faulting of this spine formed due to a lower  
689 effusion rate that resulted in more complete degassing and crystallisation that increased the magma  
690 viscosity. We advance that fluctuations in pore pressure (Farquharson et al., 2016a) and local strain  
691 rates (Coats et al., 2018; Lavallée et al., 2013; Wadsworth et al., 2019) may be especially important in  
692 triggering embrittlement of otherwise ductile magma. In the ductile regime, strain is accommodated  
693 over prolonged duration without necessarily leading to any substantial stress drop (Coats et al., 2018).  
694 Thus, under such conditions, we do not expect to detect any, or much, seismicity that would characterise  
695 magma rupture near the conduit margin (e.g., Neuberg et al., 2006; Thomas and Neuberg, 2012;  
696 Kendrick et al., 2014b). As a result, we anticipate that magma shearing below the point of rupture (ca.  
697 0.5 km at Unzen; Umakoshi et al., 2008) would have compacted and partially shut the permeability of  
698 the conduit margin, with the shear zone creating an impermeable barrier preventing gas from escaping  
699 to the surrounding country rock and promoting outgassing through the more permeable conduit core, at  
700 least up to the point of rupture (cf. Collinson and Neuberg, 2012). Upon further ascent, changes in the  
701 stress fields and physical properties of the magmas during pulsatory ascent would have favoured  
702 transition to a macroscopically brittle response to shear (Lavallée and Kendrick, 2020), triggering  
703 seismic rupture (Umakoshi et al., 2008; Lamb et al., 2015) and initiation of predominantly fault-  
704 controlled, stick-slip dynamics in the final stint of magma ascent and spine extrusion (Hornby et al.,  
705 2015). In brief periods of high discharge rate, shear may have localised along the primary seismogenic  
706 fault, simultaneously creating a Riedel fracture, but in periods with lower discharge rates, shear would  
707 have been distributed over a wide area and the fault would become inactive (stick phase), shifting the  
708 Riedel fracture to shallower depth; upon renewed discharge rate increase, shear would narrow again,  
709 and faulting would generate another Riedel fracture, and so on (Fig. 9a). Indeed, using seismic events

710 as a proxy for the ductile-brittle transition it was possible to identify its migration through time as the  
711 inclined spine loaded and compacted its lower shear zone as it grew, dilating the upper fault zone (Lamb  
712 et al., 2015). This is further indicated by the localisation of fumaroles along the upper spine margin  
713 (also observed during our latest field campaign in 2016), showing that the fault zone around the inclined  
714 spine controlled fluid circulation in the upper conduit (Lamb et al., 2015; Yamasato, 1998). Finally, a  
715 late lateral shift in dilational shearing, from the conduit margin to the conduit core, suggest that the  
716 location of shear may migrate during magma ascent in conduits as a result of changes in local stresses  
717 (e.g., upon extrusion and/ or blocks calving), likely resulting from a combination of pore pressure  
718 fluctuations, strain rate reduction and progressive inward cooling which would have favoured  
719 deformation in the core of the spine. Thus, the rheology of magma and the dominant shearing mode  
720 may evolve during ascent, which in turn dynamically modifies the permeability distribution across the  
721 conduit through time (Fig. 9a).

722

### 723 *Rheological assessment of magma switching from ductile to brittle deformation*

724 The above rheological description is primarily based on the unavoidable decompression of erupting  
725 magma (which degases, crystallises and viscously stiffens), yet previous observations at Unzen suggest  
726 that the conditions for magmatic flow may have fluctuated (Umakoshi et al., 2008; Lamb et al., 2015),  
727 thus contributing to rheological shifts. Here, we invoke findings from the literature to assess the  
728 conditions leading to rupture. The discharge rates associated with spine extrusion in 1994-95 varied,  
729 although Yamashina et al. (1999) constrained a relatively constant spine protrusion rate of  $0.8 \text{ m d}^{-1}$   
730 over a week-long period in early November 1994. Scrutinising within this period, however, seismicity  
731 indicated a pulsatory magma ascent in the conduit at shorter timescales (Umakoshi et al. 2008; Lamb  
732 et al. 2015). In particular, waveform correlation of the seismic record performed by Lamb et al. (2015)  
733 revealed rhythmic seismicity punctuated by two primary clusters that were attributed to recurring  
734 rupture associated with stick-slip cycles. They identified 668 repetitive events over the course of the 36  
735 days examined: 487 from cluster 1 and 181 from cluster 2. Progressive shallowing of cluster 1 source  
736 location was argued to result from progressive compaction of the lower shear zone (underneath the  
737 inclined magma column) as eruption slowly waned; in contrast, cluster 2, which was accompanied by  
738 low-frequency coda associated with fluid resonance, showed deepening of source location due to  
739 dilation on the overside of the inclined conduit. Considering the events in cluster 1, we define the  
740 recurrence rate of fault slip at 13.5 events per day; so each ‘stick’ interval for viscous flow would have  
741 lasted on average 106 minutes. Hornby et al. (2015) statistically analysed the slip duration of seismic  
742 events in clusters 1 and 2, defining a mode and mean of 0.1 s. In order to pursue a quantitative analysis  
743 of stick-slip behaviour, we must first turn our attention to our knowledge of Unzen magma flow and  
744 failure conditions.

745 Coats et al. (2018) studied the rheology of Unzen’s porous lavas to define a failure criterion.  
746 Considering the estimated eruptive temperature of ca. 870-900 °C (Holtz et al., 2005; Venezky and  
747 Rutherford, 1999) and measured glass transition temperature (at  $10 \text{ °C min}^{-1}$ ) of 790 °C (Wallace et al.,  
748 2019), Coats et al. (2018) empirically defined that Unzen magma would break if experiencing strain  
749 rates exceeding  $\sim 10^{-3} \text{ s}^{-1}$ ; otherwise, magma would undergo ductile flow. But these determinations were  
750 done at atmospheric pressure, so the melt was considered dry; Kusakabe et al. (1999) determined the  
751 concentration of magmatic water dissolved in the groundmass glass of eruptive products at 0.1-0.5 wt.  
752 %; however, the concentration of dissolved water at the point of rupture, at 500 m depth or  $\sim 10 \text{ MPa}$   
753 pressure considering a nominal rock density of  $\sim 2,000 \text{ kg m}^{-3}$  (Scheu et al., 2006), would have been  $\sim 1$   
754 wt. % (Liu et al., 2005). Such a higher concentration would lower the viscosity of the interstitial melt

755 one order of magnitude; as the strain rate limit shares an inverse relationship with viscosity (e.g.,  
756 Dingwell and Webb, 1989), we advance that the presence of dissolved water in the melt would have  
757 shifted the strain rate limit by approximately one order of magnitude. If we omit any upscaling of the  
758 above failure conditions for simplification and assume that deformation was localised in the  $\sim 1$  m-wide  
759 high shear area of the spine, rupture would have occurred when the ascent rate exceeded  $1 \text{ mm}\cdot\text{s}^{-1}$ . As  
760 such high deformation rate episodes are inferred to have triggered fault slip events lasting on average  
761 0.1 s (Hornby et al. 2015), each slip event may have resulted in a mere  $\geq 0.1$  mm of displacement. With  
762 13.5 events per day, this would culminate in  $\geq 1.35$  mm of magma ascent ascribed to faulting activity,  
763 signifying that deformation associated with the  $\sim 0.8$  m daily ascent was predominantly ductile and  
764 aseismic.

765 We can then turn our attention to geometrical constraints from our structural analysis to frame magma  
766 ascent conditions that satisfy the above failure criterion. The Riedel fractures that are observed at regular  
767 intervals of  $\sim 4.5$  cm in the high shear zones have been shown to be important stress and strain rate  
768 distribution markers in multiphase materials containing a weak phase, such as melt and bubbles (Finch  
769 et al., 2020), and can thus be used to constrain rates. Considering the ephemeral nature of Riedel fracture  
770 development (Finch et al., 2020), here we assume that their formation may be encouraged during brief  
771 periods of high strain rate, and they thus portray the clockwork ticking of seismogenic slip events during  
772 magma ascent. Bearing in mind an average spacing of 4.5 cm and an angle of  $57^\circ$  with respect to the  
773 main C-S fabric, we estimate the offset of the loci of rupture events at 5.4 cm. Recalling the 0.1 mm of  
774 displacement ascribed to faulting events (detailed in the previous paragraph), this suggests that ductile  
775 deformation was responsible for 5.3 cm of magma ascent during inter-seismic periods (i.e., inter-  
776 seismicity deformation, ISD; Fig 9a). Again, considering shear over 1 m area and inter-seismic periods  
777 of 106 minutes, we estimate that ductile deformation would have proceeded at an average rate of  $8 \times 10^{-6}$   
778  $\text{s}^{-1}$ ; a value well within the ductile regime as experimentally constrained by Coats et al. (2018). The  
779 above rates (of magma flow in the ductile regime and of faulting) may be conservative estimates,  
780 especially if we consider the rheological consequences of dissolved water at depth. Even if the threshold  
781 strain rate for seismogenic faulting were an order of magnitude higher, at  $10^{-2} \text{ s}^{-1}$ , this would only require  
782 13.5 mm of magma ascent in each brittle faulting event and that inter-seismic periods of ductile  
783 deformation at a rate of  $\sim 8 \times 10^{-5} \text{ s}^{-1}$  would have dominated spine extrusion.

784 In concert the physical and structural description bolstered by the rheological analysis argue for  
785 changes in magma rheology during decompression and pulsatory ascent. We propose that throughout  
786 its journey to the Earth's surface, magma may undergo several cycles of expansion (from vesiculation  
787 and dilation) and collapse (from outgassing and compaction) due to variable permeability and pore  
788 pressure, which may promote switches in shearing regimes that trigger further changes in the  
789 permeability structure of shallow conduits. For instance, the vesicles of low permeability magma may  
790 accumulate fluid, thus reducing the effective pressure and promoting brittle, dilatant rupture; rupture  
791 would in turn allow magma outgassing and a reduction in effective pressure, promoting compaction  
792 and lowering of permeability; and the cycle may recur. The picture portrayed here highlights the need  
793 to understand the coupling between magma and fluid flow dynamics and, importantly, pressure  
794 fluctuations (Michaut et al., 2013) in volcanic conduits with increased spatial and temporal complexities  
795 in order to resolve the transient state of magma and reconcile gas emission data and volcanic eruption  
796 style (Edmonds and Herd, 2007).

797

## 798 6. Conclusions

799 The present detailed study of the Mount Unzen spine reveals the competing occurrence of  
800 compactional and dilational shear regimes during magma ascent in volcanic conduits. At depth, in areas  
801 subjected to high effective pressure, shearing may induce pore compaction, thereby lowering the  
802 permeability of the system and inhibiting lateral outgassing to the country rock. At shallower depth,  
803 where the effective pressure may be low, shearing may favour localised dilation that enhances  
804 permeability. Both shear regimes result in the development of permeability anisotropy, with  
805 permeability generally being highest parallel or sub-parallel to the direction of extrusion, and lowest  
806 perpendicular to the shear plane. The observation of shearing mode overprints suggests that fluctuations  
807 in effective pressure and strain rates, during stick-slip cycles, may result in magma switching between  
808 compactant and dilational shearing regimes, thus dynamically reshaping fluid circulation at a range of  
809 scales, and in turn controlling outgassing efficiency during magma ascent and eruption.

810

### 811 **Acknowledgements**

812 We are thankful to Guðjón Eggertsson for help with the maintenance of the permeameter. This project  
813 was financially supported by a European Research Council (ERC) Starting Grant on Strain Localisation  
814 in Magma (SLiM, No. 306488) and an award from the DAIWA Anglo-Japanese Foundation (grant No.  
815 11000/11740). YL and JEK acknowledge support from the Leverhulme Trust (ECF-2016-325 and RF-  
816 2019-526\4, respectively). HT was supported by a University Research Fellowship from the Royal  
817 Society. KUH was supported by the Deutsche Forschungsgemeinschaft (DFG) project HE4565/6-1

818

### 819 **References**

- 820 Acocella, V.: Hazard mitigation of unstable volcanic edifices, *EOS*, 91, 2, 2010.  
821 Alidibirov, M., and Dingwell, D. B.: Magma fragmentation by rapid decompression, *Nature*, 380, 146-  
822 148, 1996.  
823 Ashwell, P. A., Kendrick, J. E., Lavallée, Y., Kennedy, B. M., Hess, K. U., von Aulock, F. W., Wadsworth,  
824 F. B., Vasseur, J., and Dingwell, D. B.: Permeability of compacting porous lavas, *Journal of Geophysical*  
825 *Research-Solid Earth*, 120, 1605-1622, 10.1002/2014jb011519, 2015.  
826 Baker, D. R., Brun, F., O'Shaughnessy, C., Mancini, L., Fife, J. L., and Rivers, M.: A four-dimensional X-  
827 ray tomographic microscopy study of bubble growth in basaltic foam, *Nature Communications*, 3,  
828 10.1038/ncomms2134, 2012.  
829 Ball, J. L., Stauffer, P. H., Calder, E. S., and Valentine, G. A.: The hydrothermal alteration of cooling lava  
830 domes, *Bulletin of Volcanology*, 77, 10.1007/s00445-015-0986-z, 2015.  
831 Blower, J. D.: Factors controlling permeability-porosity relationships in magma, *Bulletin of*  
832 *Volcanology*, 63, 497-504, 2001.  
833 Blundy, J., Cashman, K., and Humphreys, M.: Magma heating by decompression-driven crystallization  
834 beneath andesite volcanoes, *Nature*, 443, 76-80, 10.1038/nature05100, 2006.  
835 Brace, W. F., Walsh, J. B., and Frangos, W. T.: Permeability of granite under high pressure, *Journal of*  
836 *Geophysical Research*, 73, 2225-&, 10.1029/JB073i006p02225, 1968.  
837 Browning, J., Tuffen, H., James, M. R., Owen, J., Castro, J. M., Halliwell, S., and Wehbe, K.: Post-  
838 fragmentation vesiculation timescales in hydrous rhyolitic bombs from Chaitén volcano, *Journal of*  
839 *South American Earth Sciences*, 104, 102807, <https://doi.org/10.1016/j.jsames.2020.102807>, 2020.  
840 Burgisser, A., Chevalier, L., Gardner, J. E., and Castro, J. M.: The percolation threshold and permeability  
841 evolution of ascending magmas, *Earth and Planetary Science Letters*, 470, 37-47,  
842 10.1016/j.epsl.2017.04.023, 2017.

843 Burgisser, A., Bechon, T., Chevalier, L., Collombet, M., Arbaret, L., and Forien, M.: Conduit processes  
844 during the February 11, 2010 Vulcanian eruption of Soufriere Hills, Montserrat, *Journal of Volcanology*  
845 and *Geothermal Research*, 373, 23-35, 10.1016/j.jvolgeores.2019.01.020, 2019.

846 Caricchi, L., Burlini, L., Ulmer, P., Gerya, T., Vassalli, M., and Papale, P.: Non-Newtonian rheology of  
847 crystal-bearing magmas and implications for magma ascent dynamics, *Earth and Planetary Science*  
848 *Letters*, 264, 402-419, 2007.

849 Castro, J. M., and Gardner, J. E.: Did magma ascent rate control the explosive-effusive transition at the  
850 Inyo volcanic chain, California?, *Geology*, 36, 279-282, 10.1130/g24453a.1, 2008.

851 Castro, J. M., Cordonnier, B., Tuffen, H., Tobin, M. J., Puskar, L., Martin, M. C., and Bechtel, H. A.: The  
852 role of melt-fracture degassing in defusing explosive rhyolite eruptions at volcan Chaiten, *Earth and*  
853 *Planetary Science Letters*, 333, 63-69, 10.1016/j.epsl.2012.04.024, 2012.

854 Célarié, F., Prades, S., Bonamy, D., Ferrero, L., Bouchaud, E., Guillot, C., and Marliere, C.: Glass breaks  
855 like metal, but at the nanometer scale, *Physical Review Letters*, 90, 10.1103/PhysRevLett.90.075504,  
856 2003.

857 Chouet, B. A.: Long-period volcano seismicity: Its source and use in eruption forecasting, *Nature*, 380,  
858 309-316, 1996.

859 Coats, R., Kendrick, J. E., Wallace, P. A., Miwa, T., Hornby, A. J., Ashworth, J. D., Matsushima, T., and  
860 Lavallée, Y.: Failure criteria for porous dome rocks and lavas: a study of Mt. Unzen, Japan, *Solid Earth*,  
861 9, 1299-1328, 10.5194/se-9-1299-2018, 2018.

862 Collinson, A. S. D., and Neuberg, J. W.: Gas storage, transport and pressure changes in an evolving  
863 permeable volcanic edifice, *Journal of Volcanology and Geothermal Research*, 243, 1-13,  
864 10.1016/j.jvolgeores.2012.06.027, 2012.

865 Colombier, M., Wadsworth, F. B., Gurioli, L., Scheu, B., Kueppers, U., Di Muro, A., and Dingwell, D. B.:  
866 The evolution of pore connectivity in volcanic rocks, *Earth and Planetary Science Letters*, 462, 99-109,  
867 10.1016/j.epsl.2017.01.011, 2017.

868 Cordonnier, B., Hess, K. U., Lavallée, Y., and Dingwell, D. B.: Rheological properties of dome lavas: Case  
869 study of Unzen volcano, *Earth and Planetary Science Letters*, 279, 263-272,  
870 10.1016/j.epsl.2009.01.014, 2009.

871 Cordonnier, B., Caricchi, L., Pistone, M., Castro, J., Hess, K. U., Gottschaller, S., Manga, M., Dingwell,  
872 D. B., and Burlini, L.: The viscous-brittle transition of crystal-bearing silicic melt: Direct observation of  
873 magma rupture and healing, *Geology*, 40, 611-614, 10.1130/g3914.1, 2012.

874 Degruyter, W., Bachmann, O., Burgisser, A., and Manga, M.: The effects of outgassing on the transition  
875 between effusive and explosive silicic eruptions, *Earth and Planetary Science Letters*, 349, 161-170,  
876 10.1016/j.epsl.2012.06.056, 2012.

877 Dingwell, D. B., and Webb, S. L.: Structural relaxation in silicate melts and non-Newtonian melt  
878 rheology in geologic processes, *Physics and Chemistry of Minerals*, 16, 508-516, 1989.

879 Dingwell, D. B., and Webb, S. L.: Relaxation in silicate melts, *European Journal of Mineralogy*, 2, 427-  
880 449, 1990.

881 Dingwell, D. B.: Volcanic dilemma: flow or blow?, *Science*, 273, 1054-1055, 1996.

882 Dingwell, D. B., Lavallée, Y., Hess, K. U., Flaws, A., Martí, J., Nichols, A. R. L., Gilg, H. A., and Schillinger,  
883 B.: Eruptive shearing of tube pumice: pure and simple, *Solid Earth*, 7, 1383-1393, 10.5194/se-7-1383-  
884 2016, 2016.

885 Edmonds, M., Oppenheimer, C., Pyle, D. M., Herd, R. A., and Thompson, G.: SO<sub>2</sub> emissions from  
886 Soufriere Hills Volcano and their relationship to conduit permeability, hydrothermal interaction and  
887 degassing regime, *Journal of Volcanology and Geothermal Research*, 124, 23-43, 10.1016/s0377-  
888 0273(03)00041-6, 2003.

889 Edmonds, M., and Herd, R. A.: A volcanic degassing event at the explosive-effusive transition,  
890 *Geophysical Research Letters*, 34, 10.1029/2007gl031379, 2007.

891 Eggertsson, G. H., Lavallée, Y., Kendrick, J. E., and Markússon, S. H.: Improving fluid flow in geothermal  
892 reservoirs by thermal and mechanical stimulation: The case of Krafla volcano, Iceland, *Journal of*  
893 *Volcanology and Geothermal Research*, in press, 1-14, 2018.



894 Eichelberger, J. C., Carrigan, C. R., Westrich, H. R., and Price, R. H.: Non-explosive silicic volcanism,  
895 *Nature*, 323, 598-602, 10.1038/323598a0, 1986.

896 Farquharson, J., Heap, M. J., Varley, N. R., Baud, P., and Reuschle, T.: Permeability and porosity  
897 relationships of edifice-forming andesites: A combined field and laboratory study, *Journal of*  
898 *Volcanology and Geothermal Research*, 297, 52-68, 10.1016/j.jvolgeores.2015.03.016, 2015.

899 Farquharson, J., Heap, M. J., Baud, P., Reuschle, T., and Varley, N. R.: Pore pressure embrittlement in  
900 a volcanic edifice, *Bulletin of Volcanology*, 78, 10.1007/s00445-015-0997-9, 2016a.

901 Farquharson, J. I., Heap, M. J., and Baud, P.: Strain-induced permeability increase in volcanic rock,  
902 *Geophysical Research Letters*, 43, 11603-11610, 10.1002/2016gl071540, 2016b.

903 Farquharson, J. I., Heap, M. J., Lavallée, Y., Varley, N. R., and Baud, P.: Evidence for the development  
904 of permeability anisotropy in lava domes and volcanic conduits, *Journal of Volcanology and*  
905 *Geothermal Research*, 323, 163-185, 10.1016/j.jvolgeores.2016.05.007, 2016c.

906 Farquharson, J. I., Wadsworth, F. B., Heap, M. J., and Baud, P.: Time-dependent permeability evolution  
907 in compacting volcanic fracture systems and implications for gas overpressure, *Journal of Volcanology*  
908 *and Geothermal Research*, 339, 81-97, 10.1016/j.jvolgeores.2017.04.025, 2017.

909 Finch, M. A., Bons, P. D., Steinbach, F., Griera, A., Llorens, M.-G., Gomez-Rivas, E., Ran, H., and de  
910 Riese, T.: The ephemeral development of  $C'$  shear bands: A numerical modelling approach, *Journal of*  
911 *Structural Geology*, 139, 104091, 10.1016/j.jsg.2020.104091, 2020.

912 Fossen, H., and Cavalcante, G. C. G.: Shear zones - A review, *Earth-Science Reviews*, 171, 434-455,  
913 10.1016/j.earscirev.2017.05.002, 2017.

914 Gaunt, H. E., Sammonds, P. R., Meredith, P. G., Smith, R., and Pallister, J. S.: Pathways for degassing  
915 during the lava dome eruption of Mount St. Helens 2004-2008, *Geology*, 42, 947-950,  
916 10.1130/g35940.1, 2014.

917 Gaunt, H. E., Sammonds, P. R., Meredith, P. G., and Chadderton, A.: Effect of temperature on the  
918 permeability of lava dome rocks from the 2004-2008 eruption of Mount St. Helens, *Bulletin of*  
919 *Volcanology*, 78, 10.1007/s00445-016-1024-5, 2016.

920 Gonnermann, H. M., and Manga, M.: The fluid mechanics inside a volcano, *Annual Review of Fluid*  
921 *Mechanics*, 39, 321-356, 2007.

922 Goto, A.: A new model for volcanic earthquake at Unzen Volcano: Melt rupture model, *Geophysical*  
923 *Research Letters*, 26, 2541-2544, 1999.

924 Goto, A., Fukui, K., Hiraga, T., Nishida, Y., Ishibashi, H., Matsushima, T., Miyamoto, T., and Sasaki, O.:  
925 Rigid migration of Unzen lava rather than flow, *Journal of Volcanology and Geothermal Research*, 407,  
926 10.1016/j.jvolgeores.2020.107073, 2020.

927 Hale, A. J., and Wadge, G.: The transition from endogenous to exogenous growth of lava domes with  
928 the development of shear bands, *Journal of Volcanology and Geothermal Research*, 171, 237-257,  
929 2008.

930 Heap, M. J., Farquharson, J. I., Baud, P., Lavallée, Y., and Reuschle, T.: Fracture and compaction of  
931 andesite in a volcanic edifice, *Bulletin of Volcanology*, 77, 10.1007/s00445-015-0938-7, 2015a.

932 Heap, M. J., Kennedy, B. M., Pernin, N., Jacquemard, L., Baud, P., Farquharson, J. I., Scheu, B., Lavallee,  
933 Y., Gilg, H. A., Letham-Brake, M., Mayer, K., Jolly, A. D., Reuschle, T., and Dingwell, D. B.: Mechanical  
934 behaviour and failure modes in the Whakaari (White Island volcano) hydrothermal system, New  
935 Zealand, *Journal of Volcanology and Geothermal Research*, 295, 26-42,  
936 10.1016/j.jvolgeores.2015.02.012, 2015b.

937 Heap, M. J., and Kennedy, B. M.: Exploring the scale-dependent permeability of fractured andesite,  
938 *Earth and Planetary Science Letters*, 447, 139-150, 10.1016/j.epsl.2016.05.004, 2016.

939 Heap, M. J., Kennedy, B. M., Farquharson, J. I., Ashworth, J., Mayer, K., Letham-Brake, M., Reuschlé,  
940 T., Gilg, H. A., Scheu, B., Lavallée, Y., Sratovich, P. A., Cole, J. W., Jolly, A. D., Baud, P., and Dingwell, D.  
941 B.: A multidisciplinary approach to quantify the permeability of the Whakaari/ White Island volcanic  
942 hydrothermal system (Taupo Volcanic Zone, New Zealand), *Journal of Volcanology and Geothermal*  
943 *Research*, 10.1016/j.jvolgeores.2016.12.004, 2017a.

944 Heap, M. J., Violay, M., Wadsworth, F. B., and Vasseur, J.: From rock to magma and back again: The  
945 evolution of temperature and deformation mechanism in conduit margin zones, *Earth and Planetary  
946 Science Letters*, 463, 92-100, 10.1016/j.epsl.2017.01.021, 2017b.

947 Heap, M. J., Troll, V. R., Kushnir, A. R. L., Gilg, H. A., Collinson, A. S. D., Deegan, F. M., Darmawan, H.,  
948 Seraphine, N., Neuberg, J., and Walter, T. R.: Hydrothermal alteration of andesitic lava domes can lead  
949 to explosive volcanic behaviour, *Nature Communications*, 10, 5063, 10.1038/s41467-019-13102-8,  
950 2019.

951 Heap, M. J., and Violay, M. E. S.: The mechanical behaviour and failure modes of volcanic rocks: a  
952 review, *Bulletin of Volcanology*, 83, 10.1007/s00445-021-01447-2, 2021.

953 Heiken, G., Wohletz, K., and Eichelberger, J.: Fracture fillings and intrusive pyroclasts, Inyo domes,  
954 California, *Journal of Geophysical Research-Solid Earth and Planets*, 93, 4335-4350,  
955 10.1029/JB093iB05p04335, 1988.

956 Holland, A. S. P., Watson, I. M., Phillips, J. C., Caricchi, L., and Dalton, M. P.: Degassing processes during  
957 lava dome growth: Insights from Santiaguito lava dome, Guatemala, *Journal of Volcanology and  
958 Geothermal Research*, 202, 153-166, 10.1016/j.jvolgeores.2011.02.004, 2011.

959 Holtz, F., Sato, H., Lewis, J., Behrens, H., and Nakada, S.: Experimental petrology of the 1991-1995  
960 Unzen dacite, Japan. Part I: Phase relations, phase composition and pre-eruptive conditions, *Journal  
961 of Petrology*, 46, 319-337, 10.1093/petrology/egh077, 2005.

962 Hornby, A. J., Kendrick, J. E., Lamb, O. D., Hirose, T., De Angelis, S., von Aulock, F. W., Umakoshi, K.,  
963 Miwa, T., Henton De Angelis, S., Wadsworth, F. B., Hess, K.-U., Dingwell, D. B., and Lavallée, Y.: Spine  
964 growth and seismogenic faulting at Mt. Unzen, Japan, *Journal of Geophysical Research: Solid Earth*,  
965 120, 2169-9356, 10.1002/2014JB011660, 2015.

966 Hornby, A. J., Lavallée, Y., Kendrick, J. E., De Angelis, S., Lamur, A., Rietbrock, A., and Chigna, G.: Brittle-  
967 ductile deformation and tensile rupture of dome lava during inflation at Santiaguito, Guatemala,  
968 *Journal of Geophysical Research*, in press, 10.1029/2018JB017253, 2019.

969 Jaupart, C., and Allègre, C. J.: Gas content, eruption rate and instabilities or eruption regime in silicic  
970 volcanoes, *Earth and Planetary Science Letters*, 102, 413-429, 10.1016/0012-821x(91)90032-d, 1991.

971 Kendrick, J. E., Lavallée, Y., Ferk, A., Perugini, D., Leonhardt, R., and Dingwell, D. B.: Extreme frictional  
972 processes in the volcanic conduit of Mount St. Helens (USA) during the 2004-2008 eruption, *Journal  
973 of Structural Geology*, 38, 61-76, 10.1016/j.jsg.2011.10.003, 2012.

974 Kendrick, J. E., Lavallée, Y., Hess, K. U., Heap, M. J., Gaunt, H. E., Meredith, P. G., and Dingwell, D. B.:  
975 Tracking the permeable porous network during strain-dependent magmatic flow, *Journal of  
976 Volcanology and Geothermal Research*, 260, 117-126, 10.1016/j.jvolgeores.2013.05.012, 2013.

977 Kendrick, J. E., Lavallée, Y., Hess, K. U., De Angelis, S., Ferk, A., Gaunt, H. E., Meredith, P. G., Dingwell,  
978 D. B., and Leonhardt, R.: Seismogenic frictional melting in the magmatic column, *Solid Earth*, 5, 199-  
979 208, 10.5194/se-5-199-2014, 2014a.

980 Kendrick, J. E., Lavallée, Y., Hirose, T., Di Toro, G., Hornby, A. J., De Angelis, S., and Dingwell, D. B.:  
981 Volcanic drumbeat seismicity caused by stick-slip motion and magmatic frictional melting, *Nature  
982 Geoscience*, 7, 438-442, 10.1038/ngeo2146, 2014b.

983 Kendrick, J. E., Lavallée, Y., Varley, N. R., Wadsworth, F. B., Lamb, O. D., and Vasseur, J.: Blowing off  
984 steam: Tuffsite formation as a regulator for lava dome eruptions, *Frontiers in Earth Science*, 4,  
985 10.3389/feart.2016.00041, 2016.

986 Kendrick, J. E., Schaefer, L. N., Schaubroth, J., Bell, A. F., Lamb, O. D., Lamur, A., Miwa, T., Coats, R.,  
987 Lavallée, Y., and Kennedy, B. M.: Physical and mechanical rock properties of a heterogeneous volcano:  
988 the case of Mount Unzen, Japan, *Solid Earth*, 12, 633-664, 10.5194/se-12-1-2021, 2021.

989 Kennedy, B. M., Wadsworth, F. B., Vasseur, J., Schipper, C. I., Jellinek, A. M., von Aulock, F. W., Hess,  
990 K. U., Russell, J. K., Lavallée, Y., Nichols, A. R. L., and Dingwell, D. B.: Surface tension driven processes  
991 densify and retain permeability in magma and lava, *Earth and Planetary Science Letters*, 433, 116-124,  
992 10.1016/j.epsl.2015.10.031, 2016.

993 Kennedy, L. A., and Russell, J. K.: Cataclastic production of volcanic ash at Mount Saint Helens, *Physics  
994 and Chemistry of the Earth*, 45-46, 40-49, 10.1016/j.pce.2011.07.052, 2012.

995 Klug, C., and Cashman, K. V.: Permeability development in vesiculating magmas: Implications for  
996 fragmentation, *Bulletin of Volcanology*, 58, 87-100, 10.1007/s004450050128, 1996.

997 Kolzenburg, S., Heap, M. J., Lavallée, Y., Russell, J. K., Meredith, P. G., and Dingwell, D. B.: Strength and  
998 permeability recovery of tuffisite-bearing andesite, *Solid Earth*, 3, 191-198, 10.5194/se-3-191-2012,  
999 2012.

1000 Kueppers, U., Scheu, B., Spieler, O., and Dingwell, D. B.: Field-based density measurements as tool to  
1001 identify preeruption dome structure: set-up and first results from Unzen volcano, Japan, *Journal of*  
1002 *Volcanology and Geothermal Research*, 141, 65-75, 2005.

1003 Kusakabe, M., Sato, H., Nakada, S., and Kitamura, T.: Water contents and hydrogen isotopic ratios of  
1004 rocks and minerals from the 1991 eruption of Unzen volcano, Japan, *Journal of Volcanology and*  
1005 *Geothermal Research*, 89, 231-242, 10.1016/s0377-0273(98)00134-6, 1999.

1006 Kushnir, A. R. L., Martel, C., Bourdier, J. L., Heap, M. J., Reuschle, T., Erdmann, S., Komorowski, J. C.,  
1007 and Cholik, N.: Probing permeability and microstructure: Unravelling the role of a low-permeability  
1008 dome on the explosivity of Merapi (Indonesia), *Journal of Volcanology and Geothermal Research*, 316,  
1009 56-71, 10.1016/j.jvolgeores.2016.02.012, 2016.

1010 Kushnir, A. R. L., Martel, C., Champallier, R., and Arbaret, L.: In situ confirmation of permeability  
1011 development in shearing bubble-bearing melts and implications for volcanic outgassing, *Earth and*  
1012 *Planetary Science Letters*, 458, 315-326, 10.1016/j.epsl.2016.10.053, 2017a.

1013 Kushnir, A. R. L., Martel, C., Champallier, R., and Wadsworth, F. B.: Permeability Evolution in Variably  
1014 Glassy Basaltic Andesites Measured Under Magmatic Conditions, *Geophysical Research Letters*, 44,  
1015 10262-10271, 10.1002/2017gl074042, 2017b.

1016 Lamb, O. D., De Angelis, S., Umakoshi, K., Hornby, A. J., Kendrick, J. E., and Lavallée, Y.: Repetitive  
1017 fracturing during spine extrusion at Unzen volcano, Japan, *Solid Earth*, 6, 1277-1293, 10.5194/se-6-  
1018 1277-2015, 2015.

1019 Lamur, A., Kendrick, J. E., Eggertsson, G. H., Wall, R. J., Ashworth, J. D., and Lavallée, Y.: The  
1020 permeability of fractured rocks in pressurised volcanic and geothermal systems, *Scientific Reports*,  
1021 2017.

1022 Lamur, A., Kendrick, J. E., Wadsworth, F. B., and Lavallée, Y.: Fracture healing and strength recovery in  
1023 magmatic liquids, *Geology*, 47, 195-198, 10.1130/g45512.1, 2019.

1024 Laumonier, M., Arbaret, L., Burgisser, A., and Champallier, R.: Porosity redistribution enhanced by  
1025 strain localization in crystal-rich magmas, *Geology*, 39, 715-718, 10.1130/g31803.1, 2011.

1026 Lavallée, Y., Hess, K.-U., Cordonnier, B., and Dingwell, D. B.: Non-Newtonian rheological law for highly  
1027 crystalline dome lavas, *Geology*, 35, 843-846, 10.1130/g23594a.1, 2007.

1028 Lavallée, Y., Meredith, P. G., Dingwell, D. B., Hess, K. U., Wassermann, J., Cordonnier, B., Gerik, A., and  
1029 Kruhl, J. H.: Seismogenic lavas and explosive eruption forecasting, *Nature*, 453, 507-510,  
1030 10.1038/nature06980, 2008.

1031 Lavallée, Y., Varley, N. R., Alatorre-Ibargueñoitia, M. A., Hess, K. U., Kueppers, U., Mueller, S.,  
1032 Richard, D., Scheu, B., Spieler, O., and Dingwell, D. B.: Magmatic architecture of dome-building  
1033 eruptions at Volcan de Colima, Mexico, *Bulletin of Volcanology*, 74, 249-260, 10.1007/s00445-011-  
1034 0518-4, 2012.

1035 Lavallée, Y., Benson, P. M., Heap, M. J., Hess, K.-U., Flaws, A., Schillinger, B., Meredith, P. G., and  
1036 Dingwell, D. B.: Reconstructing magma failure and the degassing network of dome-building eruptions,  
1037 *Geology*, 41, 515-518, 10.1130/g33948.1, 2013.

1038 Lavallée, Y., Dingwell, D. B., Johnson, J. B., Cimarelli, C., Hornby, A. J., Kendrick, J. E., von Aulock, F. W.,  
1039 Kennedy, B. M., Andrews, B. J., Wadsworth, F. B., Rhodes, E., and Chigna, G.: Thermal vesiculation  
1040 during volcanic eruptions, *Nature*, 528, 544-547, 10.1038/nature16153, 2015.

1041 Lavallée, Y., and Kendrick, J. E.: A review of the physical and mechanical properties of volcanic rocks  
1042 and magmas in the brittle and ductile regimes, in: *Forecasting and planning for volcanic hazards, risks,*  
1043 *and disasters. Vol. 2, 2nd Edition ed., edited by: Papale, P., Elsevier, 2020.*

1044 Lavallée, Y., and Kendrick, J. E.: Strain localisation in magmas, in: *Magmas, Melts, Liquids and Glasses: Experimental Insights* edited by: Neuville, D. R., Henderson, G. S., and Dingwell, D. B., *Reviews in Mineralogy and Geochemistry*, Mineralogical Society of America, 2021.

1045 Lejeune, A. M., and Richet, P.: Rheology of Crystal-Bearing Silicate Melts - an Experimental-Study at High Viscosities, *Journal of Geophysical Research-Solid Earth*, 100, 4215-4229, 1995.

1046 Lejeune, A. M., Bottinga, Y., Trull, T. W., and Richet, P.: Rheology of bubble-bearing magmas, *Earth and Planetary Science Letters*, 166, 71-84, 1999.

1047 Liu, Y., Zhang, Y. X., and Behrens, H.: Solubility of H<sub>2</sub>O in rhyolitic melts at low pressures and a new empirical model for mixed H<sub>2</sub>O-CO<sub>2</sub> solubility in rhyolitic melts, *Journal of Volcanology and Geothermal Research*, 143, 219-235, 10.1016/j.jvolgeores.2004.09.019, 2005.

1048 Loiza, S., Fortin, J., Schubnel, A., Gueguen, Y., Vinciguerra, S., and Moreira, M.: Mechanical behavior and localized failure modes in a porous basalt from the Azores, *Geophysical Research Letters*, 39, 10.1029/2012gl053218, 2012.

1049 Mader, H. M., Llewellyn, E. W., and Mueller, S. P.: The rheology of two-phase magmas: A review and analysis, *Journal of Volcanology and Geothermal Research*, 257, 135-158, 10.1016/j.jvolgeores.2013.02.014, 2013.

1050 Matoza, R. S., and Chouet, B. A.: Subevents of long-period seismicity: Implications for hydrothermal dynamics during the 2004-2008 eruption of Mount St. Helens, *Journal of Geophysical Research-Solid Earth*, 115, 10.1029/2010jb007839, 2010.

1051 Melnik, O., and Sparks, R. S. J.: Nonlinear dynamics of lava dome extrusion, *Nature*, 402, 37-41, 1999.

1052 Michaut, C., Ricard, Y., Bercovici, D., and Sparks, R. S. J.: Eruption cyclicity at silicic volcanoes potentially caused by magmatic gas waves, *Nature Geoscience*, 6, 856-860, 10.1038/ngeo1928, 2013.

1053 Mueller, S., Melnik, O., Spieler, O., Scheu, B., and Dingwell, D. B.: Permeability and degassing of dome lavas undergoing rapid decompression: An experimental determination, *Bulletin of Volcanology*, 67, 526-538, 2005.

1054 Mueller, S., Scheu, B., Spieler, O., and Dingwell, D. B.: Permeability control on magma fragmentation, *Geology*, 36, 399-402, 10.1130/g24605a.1, 2008.

1055 Nakada, S., Miyake, Y., Sato, H., Oshima, O., and Fujinawa, A.: Endogenous growth of dacite dome at Unzen volcano (Japan), 1993-1994, *Geology*, 23, 157-160, 10.1130/0091-7613(1995)023<0157:egodda>2.3.co;2, 1995.

1056 Nakada, S., and Motomura, Y.: Petrology of the 1991-1995 eruption at Unzen: effusion pulsation and groundmass crystallization, *Journal of Volcanology and Geothermal Research*, 89, 173-196, 10.1016/s0377-0273(98)00131-0, 1999.

1057 Nakada, S., Shimizu, H., and Ohta, K.: Overview of the 1990-1995 eruption at Unzen Volcano, *Journal of Volcanology and Geothermal Research*, 89, 1-22, 10.1016/s0377-0273(98)00118-8, 1999.

1058 Navon, O., Chekhmir, A., and Lyakhovsky, V.: Bubble growth in highly viscous melts: theory, experiments, and autoexplosivity of dome lavas, *Earth and Planetary Science Letters*, 160, 763-776, 10.1016/s0012-821x(98)00126-5, 1998.

1059 Neuberg, J. W., Tuffen, H., Collier, L., Green, D., Powell, T., and Dingwell, D.: The trigger mechanism of low-frequency earthquakes on Montserrat, *Journal of Volcanology and Geothermal Research*, 153, 37-50, 2006.

1060 Newhall, C. G., and Melson, W. G.: Explosive activity associated with the growth of volcanic domes, *Journal of Volcanology and Geothermal Research*, 17, 111-131, 10.1016/0377-0273(83)90064-1, 1983.

1061 Ohba, T., Hirabayashi, J.-I., Nogami, K., Kusakabe, M., and Yoshida, M.: Magma degassing process during the eruption of Mt. Unzen, Japan in 1991 to 1995: Modeling with the chemical composition of volcanic gas, *Journal of Volcanology and Geothermal Research*, 175, 120-132, 10.1016/j.jvolgeores.2008.03.040, 2008.

1062 Okumura, S., Nakamura, M., and Tsuchiyama, A.: Shear-induced bubble coalescence in rhyolitic melts with low vesicularity, *Geophysical Research Letters*, 33, 10.1029/2006gl027347, 2006.

1093 Okumura, S., Nakamura, M., Tsuchiyama, A., Nakano, T., and Uesugi, K.: Evolution of bubble  
1094 microstructure in sheared rhyolite: Formation of a channel-like bubble network, *Journal of*  
1095 *Geophysical Research-Solid Earth*, 113, 10.1029/2007jb005362, 2008.

1096 Okumura, S., Nakamura, M., Takeuchi, S., Tsuchiyama, A., Nakano, T., and Uesugi, K.: Magma  
1097 deformation may induce non-explosive volcanism via degassing through bubble networks, *Earth and*  
1098 *Planetary Science Letters*, 281, 267-274, 10.1016/j.epsl.2009.02.036, 2009.

1099 Okumura, S., Nakamura, M., Nakano, T., Uesugi, K., and Tsuchiyama, A.: Shear deformation  
1100 experiments on vesicular rhyolite: Implications for brittle fracturing, degassing, and compaction of  
1101 magmas in volcanic conduits, *Journal of Geophysical Research-Solid Earth*, 115,  
1102 10.1029/2009jb006904, 2010.

1103 Okumura, S., Nakamura, M., Nakano, T., Uesugi, K., and Tsuchiyama, A.: Experimental constraints on  
1104 permeable gas transport in crystalline silicic magmas, *Contributions to Mineralogy and Petrology*, 164,  
1105 493-504, 10.1007/s00410-012-0750-8, 2012.

1106 Okumura, S., Nakamura, M., Uesugi, K., Nakano, T., and Fujioka, T.: Coupled effect of magma degassing  
1107 and rheology on silicic volcanism, *Earth and Planetary Science Letters*, 362, 163-170,  
1108 10.1016/j.epsl.2012.11.056, 2013.

1109 Okumura, S., and Sasaki, O.: Permeability reduction of fractured rhyolite in volcanic conduits and its  
1110 control on eruption cyclicity, *Geology*, 42, 843-846, 10.1130/g35855.1, 2014.

1111 Pallister, J. S., Cashman, K. V., Hagstrum, J. T., Beeler, N. M., Moran, S. C., and Denlinger, R. P.: Faulting  
1112 within the Mount St. Helens conduit and implications for volcanic earthquakes, *Geological Society of*  
1113 *America Bulletin*, 125, 359-376, 10.1130/b30716.1, 2013a.

1114 Pallister, J. S., Diefenback, A. K., Burton, W. C., Muñoz, J., Griswold, J. P., Lara, L. E., Lowenster, J. B.,  
1115 and Valenzuela, C. E.: The Chaitén rhyolite lava dome: Eruption sequence, lava dome volumes, rapid  
1116 effusion rates and source of the rhyolite magma, *Andean Geology*, 40, 277-294, 2013b.

1117 Paterson, M. S., and Wong, T.-F.: *Experimental Rock Deformation- The Brittle Field.*, Science-  
1118 *Technology*, 347p, 2005.

1119 Pistone, M., Caricchi, L., Ulmer, P., Burlini, L., Ardia, P., Reusser, E., Marone, F., and Arbaret, L.:  
1120 Deformation experiments of bubble- and crystal-bearing magmas: Rheological and microstructural  
1121 analysis, *Journal of Geophysical Research-Solid Earth*, 117, 10.1029/2011jb008986, 2012.

1122 Platz, T., Cronin, S. J., Procter, J. N., Neal, V. E., and Foley, S. F.: Non-explosive, dome-forming eruptions  
1123 at Mt. Taranaki, New Zealand, *Geomorphology*, 136, 15-30, 10.1016/j.geomorph.2011.06.016, 2012.

1124 Radon, J.: On the determination of functions from their integral values along certain manifolds, *Ieee*  
1125 *Transactions on Medical Imaging*, 5, 170-176, 10.1109/tmi.1986.4307775, 1986.

1126 Ramsay, J. G.: Shear zone geometry: A review, *Journal of Structural Geology*, 2, 83-99, 10.1016/0191-  
1127 8141(80)90038-3, 1980.

1128 Rhodes, E., Kennedy, B. M., Lavallée, Y., Hornby, A., Edwards, M., and Chigna, G.: Textural Insights Into  
1129 the Evolving Lava Dome Cycles at Santiaguito Lava Dome, Guatemala, *Frontiers in Earth Science*, 6,  
1130 10.3389/feart.2018.00030, 2018.

1131 Rohnacher, A., Rietbrock, A., Gottschämmer, E., Carter, W., Lavallée, Y., De Angelis, S., Kendrick, J. E.,  
1132 and Chigna, G.: Source mechanism of seismic explosion signals at Santiaguito volcano, Guatemala:  
1133 New insights from seismic analysis and numerical modeling, *Frontiers in Earth Science*, 8, 740,  
1134 10.3389/feart.2020.603441 2021.

1135 Rust, A. C., and Manga, M.: Bubble shapes and Orientations in low Re simple shear flow, *Journal of*  
1136 *Colloid and Interface Science*, 249, 476-480, 10.1006/jcis.2002.8292, 2002.

1137 Rust, A. C., Manga, M., and Cashman, K. V.: Determining flow type, shear rate and shear stress in  
1138 magmas from bubble shapes and orientations, *Journal of Volcanology and Geothermal Research*, 122,  
1139 111-132, 2003.

1140 Rust, A. C., and Cashman, K. V.: Permeability of vesicular silicic magma: inertial and hysteresis effects,  
1141 *Earth and Planetary Science Letters*, 228, 93-107, 2004.

1142 Rust, A. C., and Cashman, K. V.: Permeability controls on expansion and size distributions of pyroclasts,  
1143 *Journal of Geophysical Research-Solid Earth*, 116, 17, 10.1029/2011jb008494, 2011.

1144 Rutter, E. H.: On the nomenclature of mode of failure transitions in rocks, *Tectonophysics*, 122, 381-  
1145 387, 10.1016/0040-1951(86)90153-8, 1986.

1146 Ryan, A. G., Heap, M. J., Russell, J. K., Kennedy, L. A., and Clyne, M. A.: Cyclic shear zone cataclasis  
1147 and sintering during lava dome extrusion: Insights from Chaos Crags, Lassen Volcanic Center (USA),  
1148 *Journal of Volcanology and Geothermal Research*, 401, 10.1016/j.jvolgeores.2020.106935, 2020.

1149 Sahagian, D.: Volcanology - Magma fragmentation in eruptions, *Nature*, 402, 589+, 1999.

1150 Sahetapy-Engel, S. T., and Harris, A. J. L.: Thermal structure and heat loss at the summit crater of an  
1151 active lava dome, *Bulletin of Volcanology*, 71, 15-28, 10.1007/s00445-008-0204-3, 2009.

1152 Sato, H., Suto, S., Ui, T., Fujii, T., Yamamoto, T., Takarada, S., and Sakaguchi, K.: Flowage of the 1991  
1153 Unzen lava; discussions to Goto et al., 2020 'Rigid migration of Unzen lava rather than flow' *J. Volcanol.*  
1154 *Geotherm. Res.*, 110, 107073, *Journal of Volcanology and Geothermal Research*, 107343,  
1155 <https://doi.org/10.1016/j.jvolgeores.2021.107343>, 2021.

1156 Saubin, E., Kennedy, B., Tuffen, H., Villeneuve, M. C., Davidson, J., and Burchardt, S.: Comparative field  
1157 study of shallow rhyolite intrusions in Iceland: Emplacement mechanisms and impact on country  
1158 rocks, *Journal of Volcanology and Geothermal Research*, 388, 106691,  
1159 <https://doi.org/10.1016/j.jvolgeores.2019.106691>, 2019.

1160 Schaefer, L. N., Kennedy, B. M., Kendrick, J. E., Lavallée, Y., and Miwa, T.: Laboratory Measurements  
1161 of Damage Evolution in Dynamic Volcanic Environments: From Slow to Rapid Strain Events, 54th U.S.  
1162 Rock Mechanics/Geomechanics Symposium, 2020,

1163 Scheu, B., Spieler, O., and Dingwell, D. B.: Dynamics of explosive volcanism at Unzen volcano: an  
1164 experimental contribution, *Bulletin of Volcanology*, 69, 175-187, 2006.

1165 Scheu, B., Kueppers, U., Mueller, S., Spieler, O., and Dingwell, D. B.: Experimental volcanology on  
1166 eruptive products of Unzen, *Journal of Volcanology and Geothermal Research*, 175, 110-119,  
1167 10.1016/j.jvolgeores.2008.03.023, 2007.

1168 Shields, J. K., Mader, H. M., Pistone, M., Caricchi, L., Floess, D., and Putlitz, B.: Strain-induced  
1169 outgassing of three-phase magmas during simple shear, *Journal of Geophysical Research-Solid Earth*,  
1170 119, 6936-6957, 10.1002/2014jb011111, 2014.

1171 Smith, J. V., Miyake, Y., and Oikawa, T.: Interpretation of porosity in dacite lava domes as ductile-  
1172 brittle failure textures, *Journal of Volcanology and Geothermal Research*, 112, 25-35, 10.1016/s0377-  
1173 0273(01)00232-3, 2001.

1174 Smith, J. V.: Structural analysis of flow-related textures in lavas, *Earth-Science Reviews*, 57, 279-297,  
1175 Pii s0012-8252(01)00081-2  
1176 10.1016/s0012-8252(01)00081-2, 2002.

1177 Sparks, R. S. J.: Causes and consequences of pressurisation in lava dome eruptions, *Earth and Planetary*  
1178 *Science Letters*, 150, 177-189, 1997.

1179 Sparks, R. S. J., Murphy, M. D., Lejeune, A. M., Watts, R. B., Barclay, J., and Young, S. R.: Control on the  
1180 emplacement of the andesite lava dome of the Soufriere Hills volcano, Montserrat by degassing-  
1181 induced crystallization, *Terra Nova*, 12, 14-20, 2000.

1182 Sparks, R. S. J.: Dynamics of magma degassing, in: *Volcanic Degassing*, edited by: Oppenheimer, C.,  
1183 Pyle, D. M., and Barclay, J., Geological Society Special Publication, 5-22, 2003.

1184 Stasiuk, M. V., Barclay, J., Carroll, M. R., Jaupart, C., Ratte, J. C., Sparks, R. S. J., and Tait, S. R.: Degassing  
1185 during magma ascent in the Mule Creek vent (USA), *Bulletin of Volcanology*, 58, 117-130, 1996.

1186 Stix, J., Layne, G. D., and Williams, S. N.: Mechanisms of degassing at Nevado del Ruiz volcano,  
1187 Colombia, *Journal of the Geological Society*, 160, 507-521, 2003.

1188 Tait, S., Jaupart, C., and Vergnolle, S.: Pressure, gas content and eruption periodicity of a shallow,  
1189 crystallizing magma chamber, *Earth and Planetary Science Letters*, 92, 107-123, 10.1016/0012-  
1190 821x(89)90025-3, 1989.

1191 Thomas, M. E., and Neuberg, J.: What makes a volcano tick--A first explanation of deep multiple  
1192 seismic sources in ascending magma, *Geology*, 40, 351-354, 10.113/G32868.1, 2012.

1193 Tiab, D., and Donaldson, E. C.: Chapter 3 - Porosity and Permeability, in: *Petrophysics (Fourth Edition)*,  
1194 edited by: Tiab, D., and Donaldson, E. C., Gulf Professional Publishing, Boston, 67-186, 2016.

1195 Tuffen, H., Dingwell, D. B., and Pinkerton, H.: Repeated fracture and healing of silicic magma generate  
1196 flow banding and earthquakes?, *Geology*, 31, 1089-1092, 2003.

1197 Tuffen, H., and Dingwell, D. B.: Fault textures in volcanic conduits: evidence for seismic trigger  
1198 mechanisms during silicic eruptions, *Bulletin of Volcanology*, 67, 370-387, 2005.

1199 Umakoshi, K., Takamura, N., Shinzato, N., Uchida, K., Matsuwo, N., and Shimizu, H.: Seismicity  
1200 associated with the 1991-1995 dome growth at Unzen Volcano, Japan, *Journal of Volcanology and  
1201 Geothermal Research*, 175, 91-99, 10.1016/j.jvolgeores.2008.03.030, 2008.

1202 Varley, N. R., and Taran, Y.: Degassing processes of popocatepetl and Volcan de Colima, Mexico, in:  
1203 *Volcanic Degassing*, edited by: Oppenheimer, C. P. D. M. B. J., Geological Society Special Publication,  
1204 263-280, 2003.

1205 Vasseur, J., Wadsworth, F. B., Lavallée, Y., Hess, K.-U., and Dingwell, D. B.: Volcanic sintering:  
1206 Timescales of viscous densification and strength recovery, *Geophysical Research Letters*, 40, 5658-  
1207 5664, 10.1002/2013gl058105, 2013.

1208 Venezky, D. Y., and Rutherford, M. J.: Petrology and Fe-Ti oxide reequilibration of the 1991 Mount  
1209 Unzen mixed magma, *Journal of Volcanology and Geothermal Research*, 89, 213-230, 10.1016/s0377-  
1210 0273(98)00133-4, 1999.

1211 Wadsworth, F. B., Vasseur, J., von Aulock, F. W., Hess, K.-U., Scheu, B., Lavallée, Y., and Dingwell, D.  
1212 B.: Nonisothermal viscous sintering of volcanic ash, *Journal of Geophysical Research-Solid Earth*, 119,  
1213 8792-8804, 10.1002/2014jb011453, 2014.

1214 Wadsworth, F. B., Vasseur, J., Scheu, B., Kendrick, J. E., Lavallée, Y., and Dingwell, D. B.: Universal  
1215 scaling of fluid permeability during volcanic welding and sediment diagenesis, *Geology*, 44, 219-222,  
1216 10.1130/g37559.1, 2016.

1217 Wadsworth, F. B., Vasseur, J., Llewellyn, E. W., Dobson, K. J., Colombier, M., von Aulock, F. W., Fife, J.  
1218 L., Wiesmaier, S., K.-U., H., Scheu, B., Lavallée, Y., and Dingwell, D. B.: Topological inversions in  
1219 coalescing granular media control fluid-flow regimes, *PHYSICAL REVIEW E*, 96, 033113, 2017.

1220 Wadsworth, F. B., Witcher, T., Vossen, C. E. J., Hess, K.-U., Unwin, H. E., Scheu, B., Castro, J. M., and  
1221 Dingwell, D. B.: Combined effusive-explosive silicic volcanism straddles the multiphase viscous-to-  
1222 brittle transition, *Nature Communications*, 9, 10.1038/s41467-018-07187-w, 2018.

1223 Wadsworth, F. B., Witcher, T., Vasseur, J., Dingwell, D. B., and Scheu, B.: When Does Magma Break?,  
1224 in: *Volcanic Unrest: From Science to Society*, edited by: Gottsmann, J., Neuberg, J., and Scheu, B.,  
1225 *Advances in Volcanology*, 171-184, 2019.

1226 Wadsworth, F. B., Vasseur, J., Llewellyn, E. W., Brown, R. J., Tuffen, H., Gardner, J. E., Kendrick, J. E.,  
1227 Lavallée, Y., Dobson, K. J., Heap, M. J., Dingwell, D. B., Hess, K.-U., Schaubroth, J., von Aulock, F. W.,  
1228 Kushnir, A. R. L., and Marone, F.: A model for permeability evolution during volcanic welding, *Journal  
1229 of Volcanology and Geothermal Research*, 409, 107118,  
1230 <https://doi.org/10.1016/j.jvolgeores.2020.107118>, 2021.

1231 Wallace, P. A., Kendrick, J. E., Ashworth, J. D., Miwa, T., Coats, R., De Angelis, S. H., Mariani, E., Utley,  
1232 J. E. P., Biggin, A., Kendrick, R., Nakada, S., Matsushima, T., and Lavallée, Y.: Petrological architecture  
1233 of a magmatic shear zone: A multidisciplinary investigation of strain localisation during magma ascent  
1234 at Unzen Volcano, Japan, *Journal of Petrology*, 60, 791-826, 10.1093/petrology/egz016, 2019.

1235 Watanabe, T., Shimizu, Y., Noguchi, S., and Nakada, S.: Permeability measurements on rock samples  
1236 from Unzen scientific drilling project drill hole 4 (USDP-4), *Journal of Volcanology and Geothermal  
1237 Research*, 175, 82-90, 10.1016/j.jvolgeores.2008.03.021, 2008.

1238 Watts, R. B., Herd, R. A., Sparks, R. S. J., and Young, S. R.: Growth patterns and emplacement of the  
1239 andesitic lava dome at Soufriere Hills Volcano, Montserrat, in: *Eruption of Soufriere Hills Volcano,  
1240 Montserrat, from 1995 to 1999*, edited by: Druitt, T. H., and Kokelaar, P., 21, Geological Society of  
1241 London Memoir, 115-152, 2002.

1242 Westrich, H. R., and Eichelberger, J. C.: Gas transport and bubble collapse in rhyolitic magma - an  
1243 experimental approach, *Bulletin of Volcanology*, 56, 447-458, 10.1007/bf00302826, 1994.

1244 Woods, A. W., and Koyaguchi, T.: Transitions between explosive and effusive eruptions of silicic  
1245 magmas, *Nature*, 370, 641-644, 1994.

1246 Wright, H. M. N., Roberts, J. J., and Cashman, K. V.: Permeability of anisotropic tube pumice: Model  
1247 calculations and measurements, *Geophysical Research Letters*, 33, 10.1029/2006gl027224, 2006.  
1248 Wright, H. M. N., and Weinberg, R. F.: Strain localization in vesicular magma: Implications for rheology  
1249 and fragmentation, *Geology*, 37, 1023-1026, 10.1130/g30199a.1, 2009.  
1250 Yamasato, H.: Nature of infrasonic pulse accompanying low frequency earthquake at Unzen volcano,  
1251 Japan, *Bulletin of the volcanological society of Japan*, 43, 1-13, 10.18940/kazan.43.1\_1, 1998.  
1252 Yamashina, K., Matsushima, T., and Ohmi, S.: Volcanic deformation at Unzen, Japan, visualized by a  
1253 time-differential stereoscopy, *Journal of Volcanology and Geothermal Research*, 89, 73-80,  
1254 10.1016/s0377-0273(98)00124-3, 1999.  
1255 Yilmaz, T. I., Wadsworth, F. B., Gilg, H. A., Hess, K. U., Kendrick, J. E., Wallace, P. A., Lavallée, Y., Utley,  
1256 J. E. P., Vasseur, J., Nakada, S., and Dingwell, D. B.: Rapid alteration of fractured volcanic conduits  
1257 beneath Mt Unzen, *Bulletin of Volcanology*, 83, 34, 2021.  
1258 Yoshimura, S., and Nakamura, M.: Fracture healing in a magma: An experimental approach and  
1259 implications for volcanic seismicity and degassing, *Journal of Geophysical Research-Solid Earth*, 115,  
1260 10.1029/2009jb000834, 2010.  
1261 Zhang, Y. X.: H<sub>2</sub>O in rhyolitic glasses and melts: Measurement, speciation, solubility, and diffusion,  
1262 *Reviews of Geophysics*, 37, 493-516, 1999.

1263

1264



1265 **Figure Caption**

1266 Figure 1. a) Google Earth image showing the location of Unzen volcano on the island of Kyushu,  
1267 Japan. b) Photograph of Unzen volcano, looking northwest, viewed from near Onokoba in the suburbs  
1268 of Shimabara city. c) Photo of the relict 1994–95 spine at Unzen volcano (looking westward), showing  
1269 (I) the central shear zone (i.e., the cavitation structures detailed in Smith *et al.*, 2001, further expanded  
1270 in the inset); (II) the marginal shear zone, bordered by a fault (dark orange-brown colour), and (III) a  
1271 large block of sintered breccia of earlier domes, which has become welded to the fault material and  
1272 extruded with the spine. Adapted from Hornby *et al.* (2015). d) Photograph of a fragment of the spine  
1273 showing the primary internal structure of the shear zone, bordered by a set of closely spaced, inclined  
1274 fractures to the left and indurated breccia to the right.

1275

1276 Figure 2. Location of the lava spine blocks and characteristics of the marginal shear zone. a) An aerial  
1277 view of Unzen lava dome summit showing the remnants of the 1994-95 lava spine, including the main  
1278 spine, the central shear zone (CSZ) block and the marginal shear zone (MSZ) block. b) Photograph of  
1279 the main spine inclined towards the east. c) 3D construction of the marginal shear zone block (created  
1280 using the photogrammetry 3DF Zephyr by 3Dflow). The outcrop is annotated to show the location of  
1281 samples (A-H) as well as the 4 main regions (gouge as well as high-, moderate- and low-shear zones)  
1282 and key features, including the fault contact (red dashed curve), shear zone transitions (yellow dashed  
1283 curves), extension of tensile fracture (C; green lines) and Riedel fractures (blue curves). The inset  
1284 shows detail of the fault plane, dividing the gouge and high-shear zone. Directional arrows X, Y and  
1285 Z show the orientation of sample coring relative to the shear plane. d) View of the MSZ block parallel  
1286 to the shear plane and perpendicular to the shear plane. Insets show surface textures across the shear  
1287 zone.

1288

1289 Figure 3. Composite figure of the microtextural characteristics across the marginal shear zone  
1290 consisting of photograph of fresh surface textures, plane polarised light (PPL) photomicrographs,  
1291 ultraviolet (UV) light photomicrographs and backscattered electron (BSE) images of the groundmass.  
1292 Images of the fresh surface were taken following cutting the sample perpendicular to shear. The C-  
1293 fabric (red line) and S-fabrics (dashed yellow line) are labelled in gouge, high shear and moderate  
1294 shear zones. The C-fabric runs consistently parallel to the shear direction, while the S-fabric is slightly  
1295 inclined to variable degrees across the MSZ. Phenocryst observed include plagioclase (P), amphibole  
1296 (A), biotite (B) and quartz (Q). Green boxes on PPL photomicrographs show the location of the UV  
1297 light images, which highlight the pore structures across the MSZ. On UV light images, two white  
1298 arrows pointing away from each other show the location of fractures within the groundmass (samples  
1299 G and H), single arrows point to large pores adjacent to large phenocryst (samples G and H), and two  
1300 arrows pointing towards each other show compaction bands (their spacing represents the width of  
1301 each band; samples B and C). In the BSE images, a porous diktytaxitic texture is prevalent across the  
1302 shear zone, although in the high shear zones (samples B and C) these textures are impeded by low-  
1303 porosity compaction bands that show strong crystal alignment, fractured crystals (FC), and pulverised  
1304 crystal band (PCB).

1305

1306 Figure 4. Tomographic reconstructions of four samples across the shear zones: a-b) A, c-d) C, e-f) E,  
1307 g-h) H.; The upper row shows density-based images of tomographic reconstructions, whereas the  
1308 lower row highlights the porous network in blue and the solid fraction is transparent. The

1309 reconstruction shows that the porous fraction becomes increasingly localised towards the fault plane  
1310 (i.e., from right to left).

1311

1312 Figure 5. a) Porosity and permeability (parallel and perpendicular to shear plane) profile across the  
1313 shear zone (at  $P_{eff} \approx 5$  MPa), showing the compactant (ductile) nature of the high shear zone,  
1314 overprint by localised, dilational (brittle) fractures. Measurements on the gouge sample are plotted at  
1315 a distance of 0 m. b) Porosity reduction as a function of effective pressure, derived from the volume  
1316 of water expelled during loading in effective pressure of samples cored parallel to shear. Note that the  
1317 initial porosity value (at  $P_{eff} \approx 5$  MPa) is that of the sample initial porosity (before loading); the exact  
1318 quantity of volume expelled between 0.1 and 5MPa cannot be accurately determined due to the  
1319 method used, hence we simply show the porosity reduction from this point onward.

1320

1321 Figure 6. Permeability of the marginal shear zone as a function of effective pressure and direction to  
1322 shear: measurements conducted a) parallel and b) perpendicular to the shear plane. The data shows a  
1323 reduction in permeability with effective pressure; yet the permeability profile across the shear zone  
1324 remains, irrespective of the pressure conditions tested. The data shows contrasting permeabilities as a  
1325 function of direction, which create c) permeability anisotropy, cast here as the ratio between the  
1326 permeability parallel and perpendicular to the shear plane. The anisotropy is most pronounced in the  
1327 high shear zone and generally increases as samples were loaded to higher effective pressure due to  
1328 fracture closure. Note that the x-axis was truncated and the scale was expanded for the near-fault  
1329 high-shear zone for which we conducted more measurements due to the structurally complex nature  
1330 of this area of the spine. Measurements on the gouge sample are plotted at a distance of 0 m.

1331

1332 Figure 7. a) Photograph showing measurement locations for the field-based permeability  
1333 measurements, for the upper (orange) and lower (green) transects. b) Permeability data for the upper  
1334 (orange) and lower (green) transects, plotted against distance. The data shows a drastic increase in  
1335 permeability of  $\sim 3$  orders of magnitude.

1336

1337 Figure 8. Permeability-porosity relationship for Unzen dome lavas and similar effusive lavas. Blue  
1338 and red circles represent data from this study, made parallel and perpendicular to the plane of shear,  
1339 respectively. Grey circles show porosity data for Unzen from Mueller *et al.* (2005) and Kendrick *et al.*  
1340 (2021), and open circles show permeability measurement on USDP drill cores from Watanabe *et al.*  
1341 (2008). Other symbols show data for effusive products at similar dome eruptions.

1342

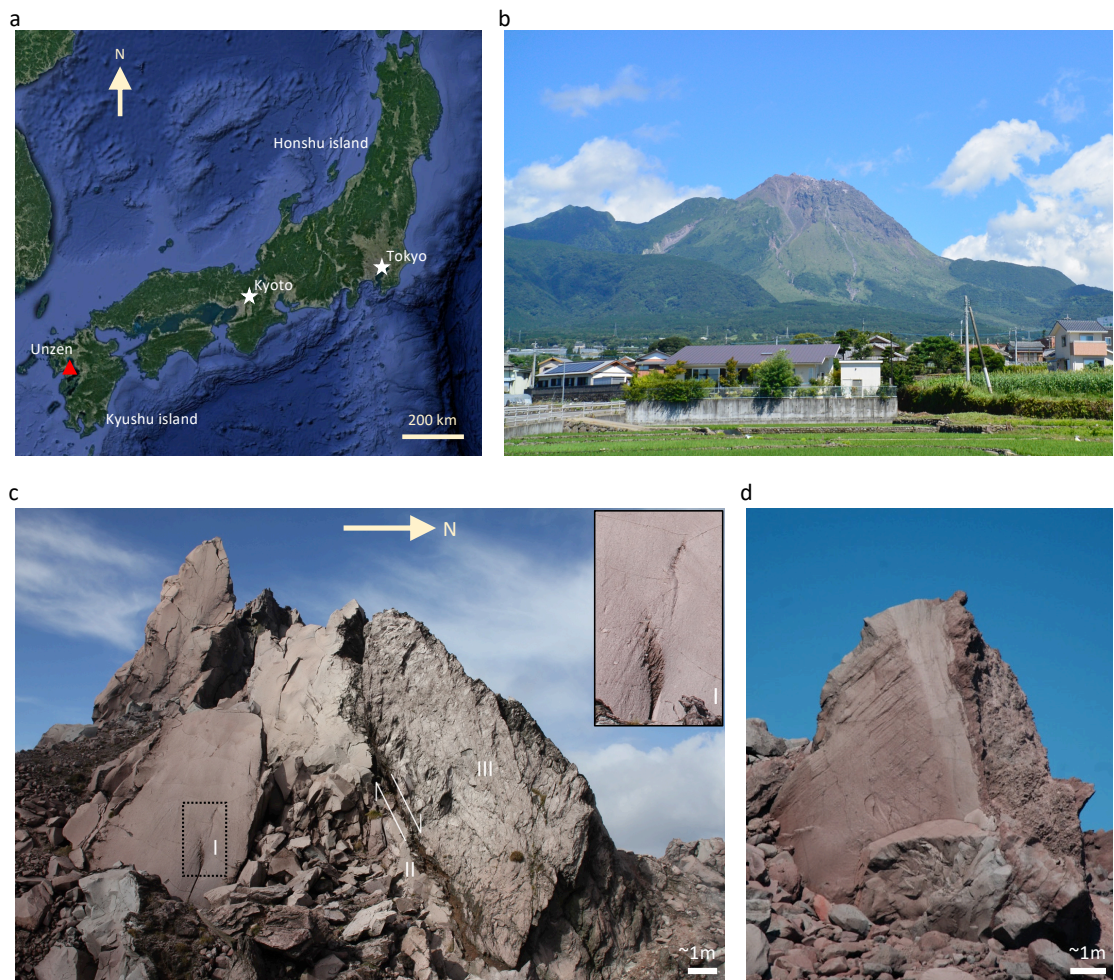
1343 Figure 9. a) Conceptual model showing rheological shifts and evolution of permeability (seen as fluid  
1344 flow vectors) during pulsatory magma ascent and stick-slip faulting. The sketches illustrate the  
1345 evolution of the extent of active shear zones (in orange), inactive areas (dark reds), active faults (blue)  
1346 and inactive faults (grey), during magma discharge fluctuations. The dominant rheology in each area  
1347 is numbered (1-4) and is linked to the deformation mechanism map for magma (shown in b). The  
1348 sketches (a) show that shear narrows toward the eruption point as magmas is subjected to lower  
1349 effective pressure (as shown in b). Compaction of the outer margin of the shear zones (dark red-  
1350 brown) would generate a zone of lower permeability (which may act as a local fluid flow barrier) As  
1351 discharge rates increase, the width of the shear zone also narrows, and promote a switch to brittle  
1352 failure at shallow depth ( $\sim 500$  m), causing the propagation of a primary fault plane and an adjacent

1353 Riedel fracture (which channels fluid flow; blue arrow). Upon discharge rate reduction, the shear zone  
1354 would widen again and the fault would become inactive (stick phase), shifting the Riedel fracture to  
1355 shallower depth. Upon renewed discharge rate increase, shear would narrow again, and faulting would  
1356 generate another Riedel fracture. Thus, the distance between Riedel fractures may be used to resolve  
1357 the magma ascent associated with inter-seismicity deformation (ISD). b) Sketch of a deformation  
1358 mechanism map for magma (adapted from Lavallée and Kendrick, 2020). At low differential stresses  
1359 magma flows viscously, but at higher differential stresses, magma may undergo the glass transition  
1360 and the deformation mode may switch to brittle rupture (dilatant shear) or ductile cataclastic flow  
1361 (compactant shear), depending on the effective mean stress. These deformation modes form yield  
1362 caps, displayed by blue and green lines representing brittle rupture and ductile cataclastic flow,  
1363 respectively. Each line refers to a given strain rate condition and the sketch shows an increase in  
1364 strength as a function of strain rate ( $\dot{\epsilon}$ ); in brittle field, strain rate may increase with differential stress  
1365 and/ or by lowering the effective mean stress, whilst in the ductile field, the strain rate may increase  
1366 with differential stress as well as effective mean stress. The inset double-head arrow indicates  
1367 magmatic scenarios which may influence the effective mean stress: for instance, decompression or  
1368 pore pressurisation may reduce the effective mean stress whilst outgassing may increase it. The  
1369 numbers refer to scenarios as displayed for different parts of the magmatic column in panel (a).

1370

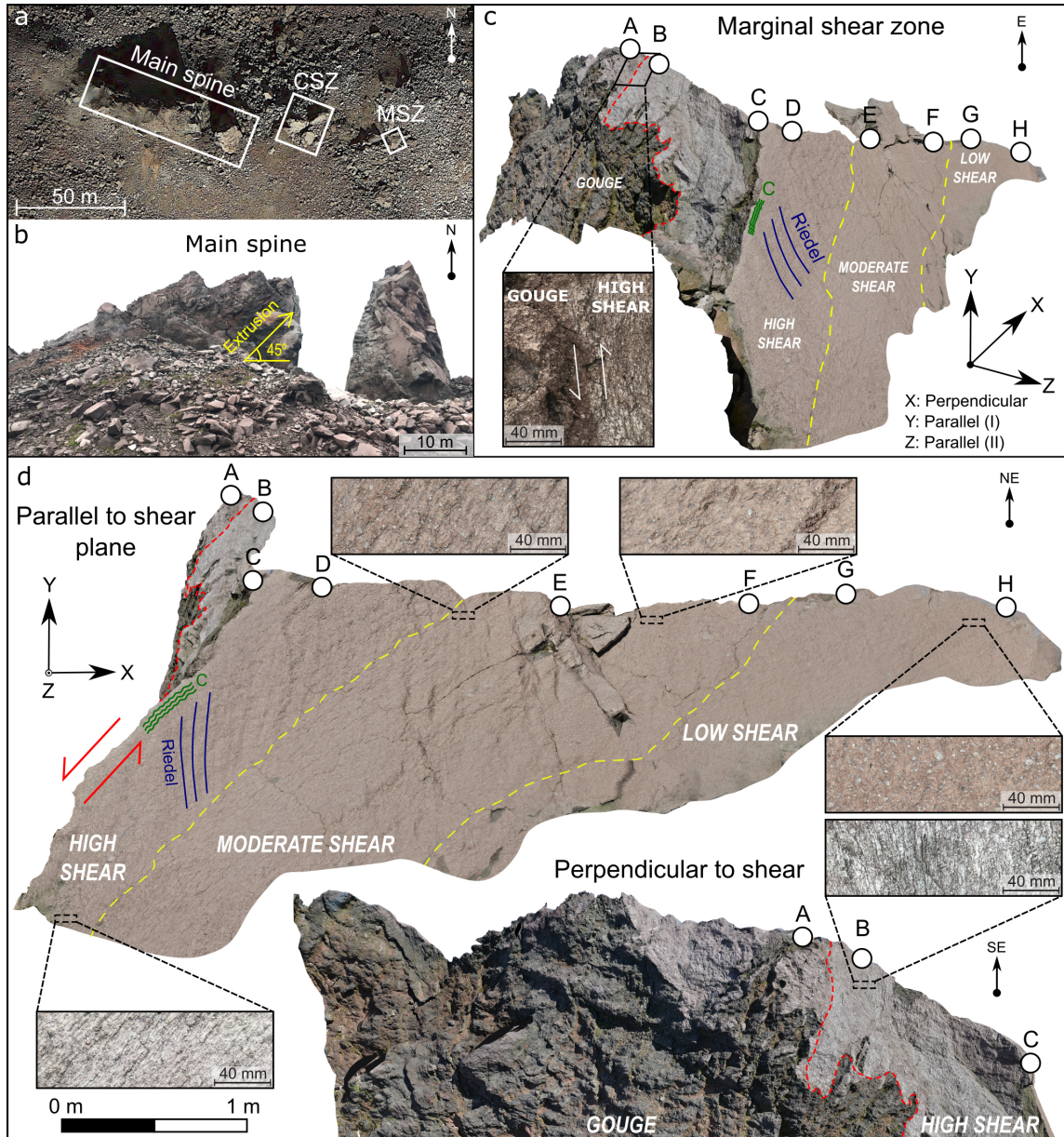
1371 Figure 1

1372





1373 Figure 2

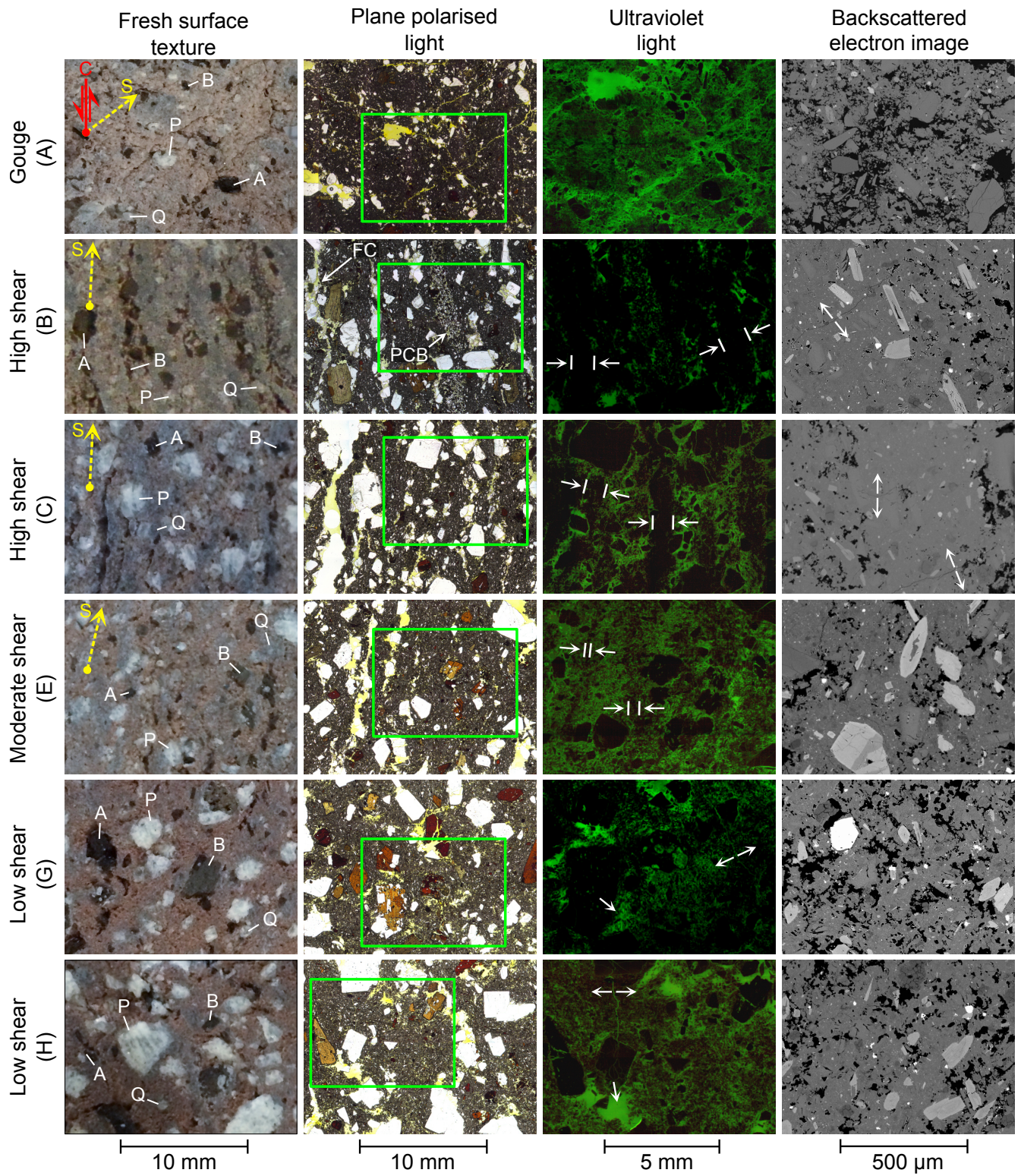


1374

1375



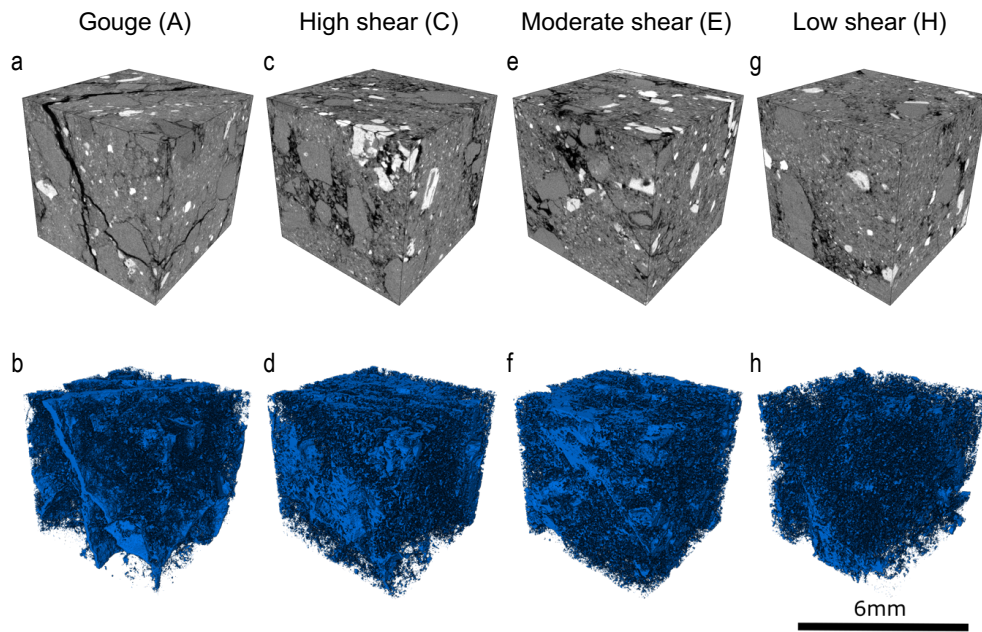
1376 Figure 3



1377

1378

1379 Figure 4

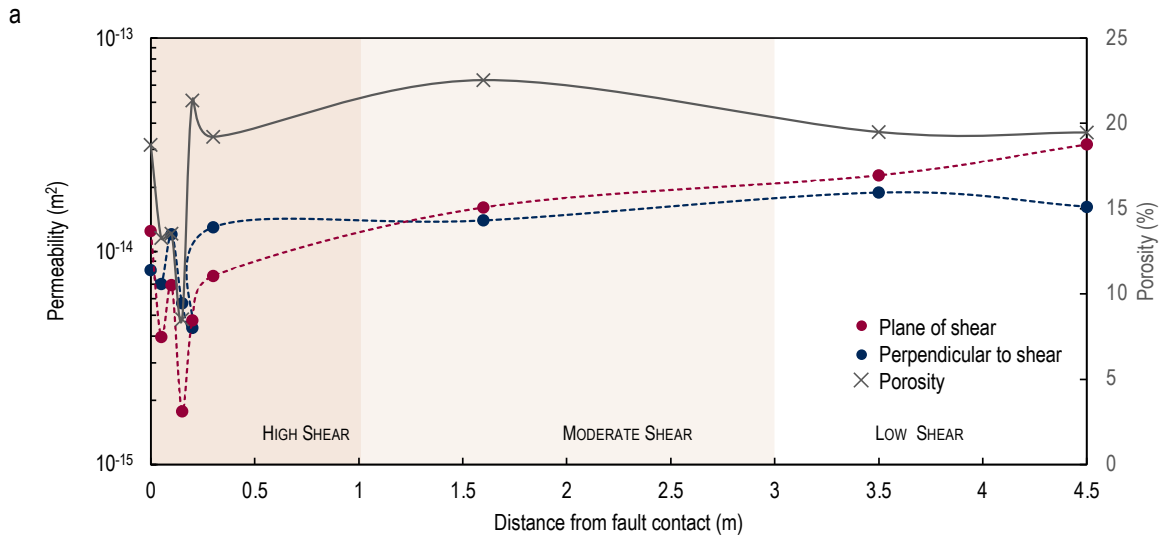


1380

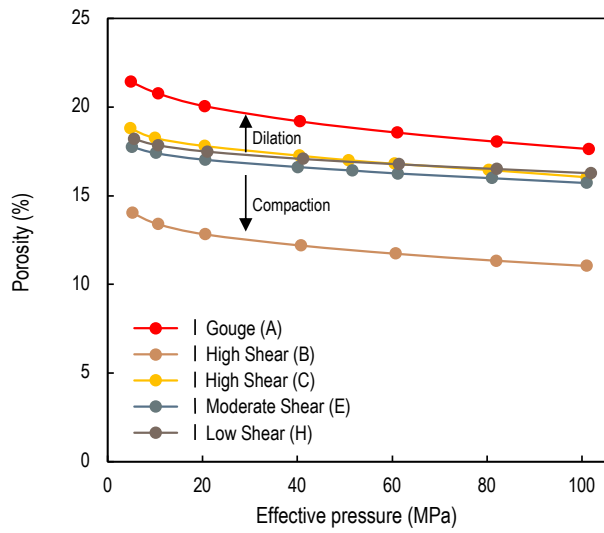
1381

1382 Figure 5

1383



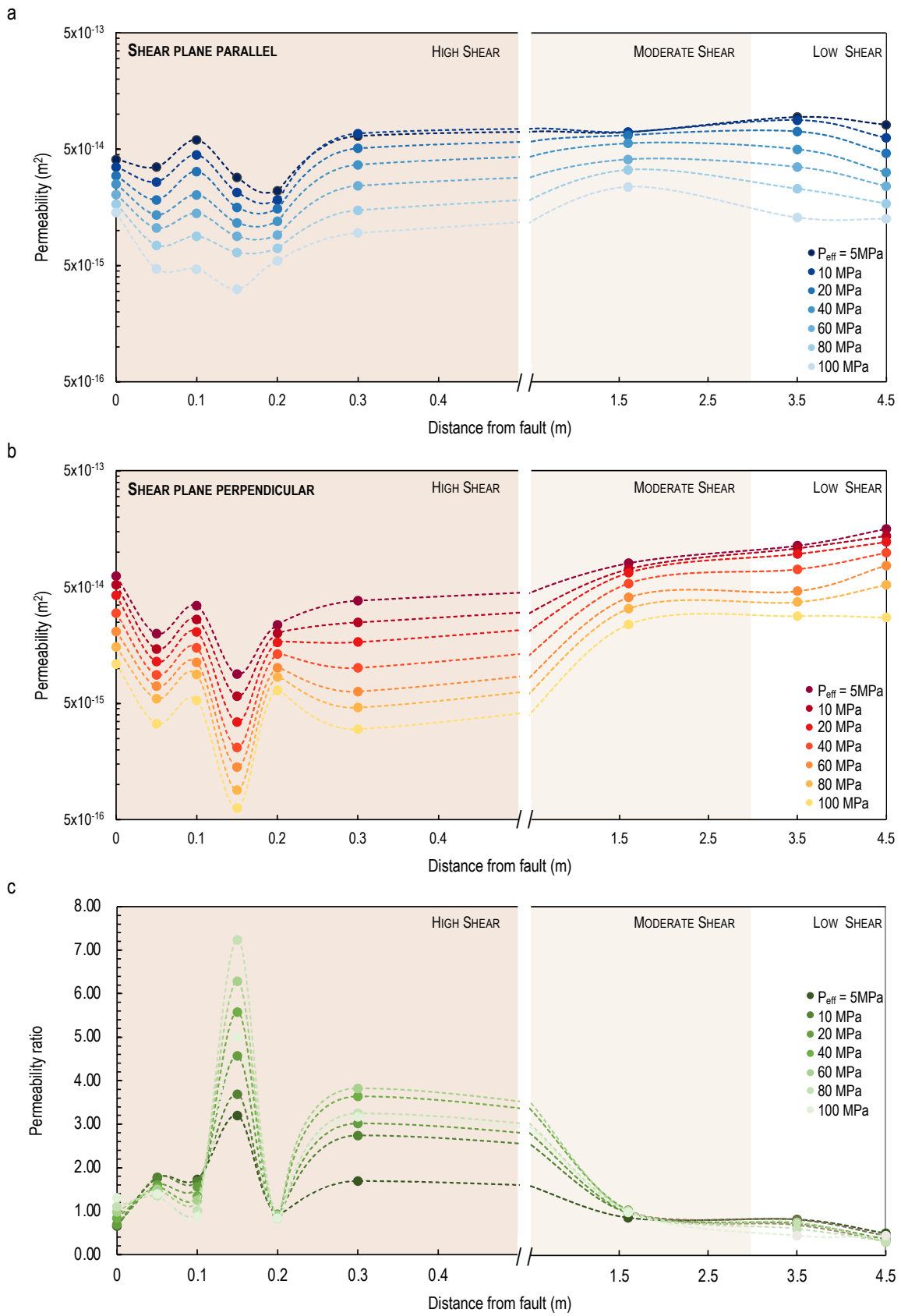
b



1384

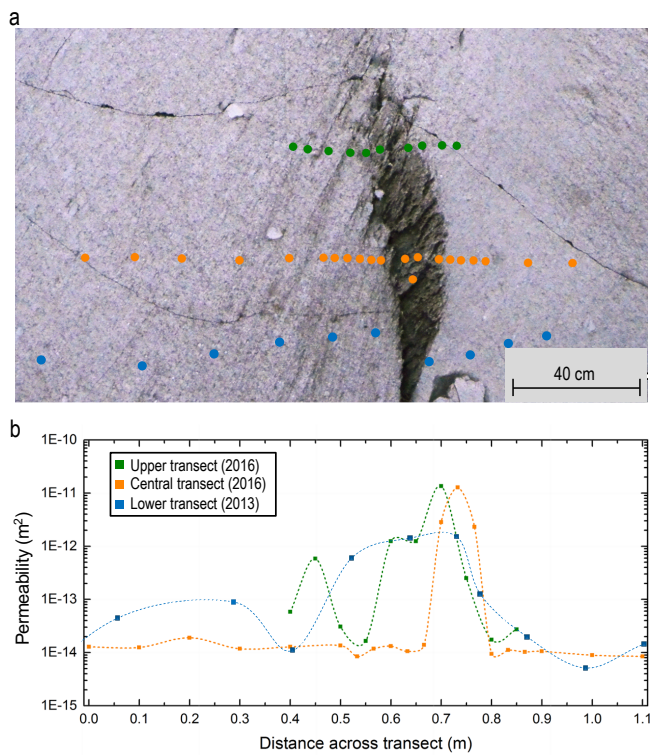


1385 Figure 6

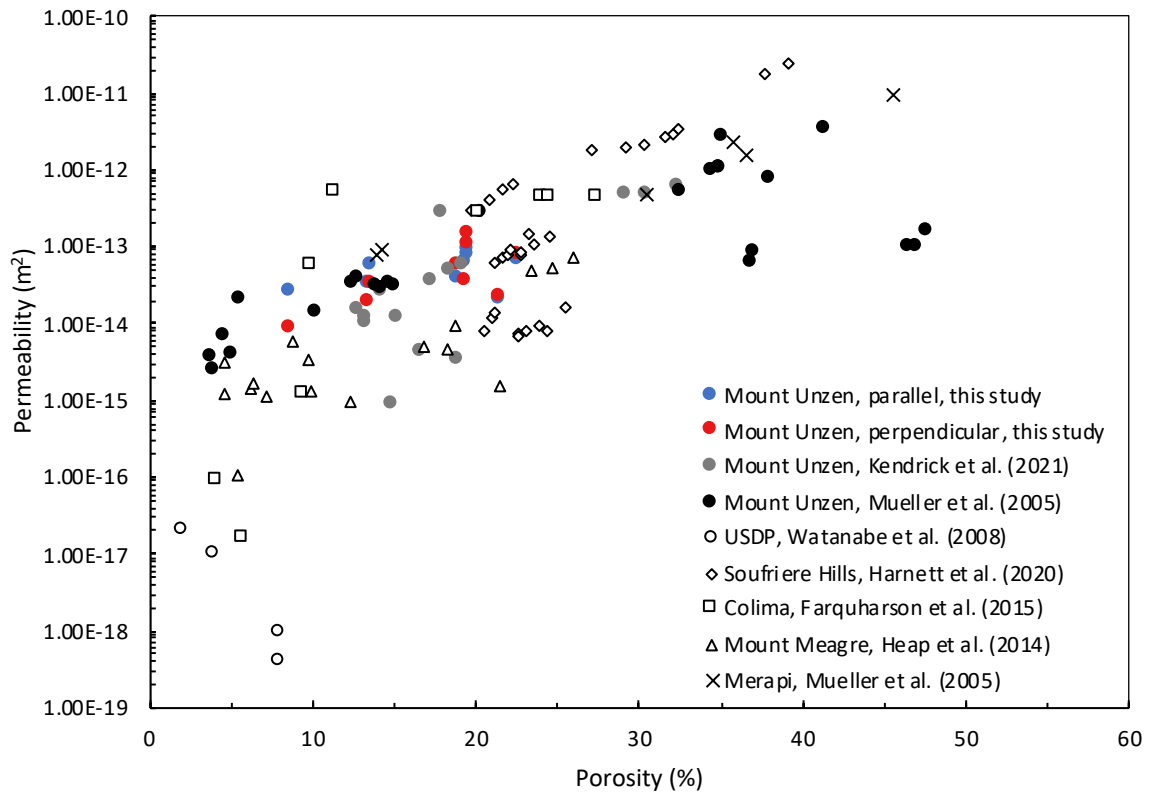


1386

1387



1391 Figure 8

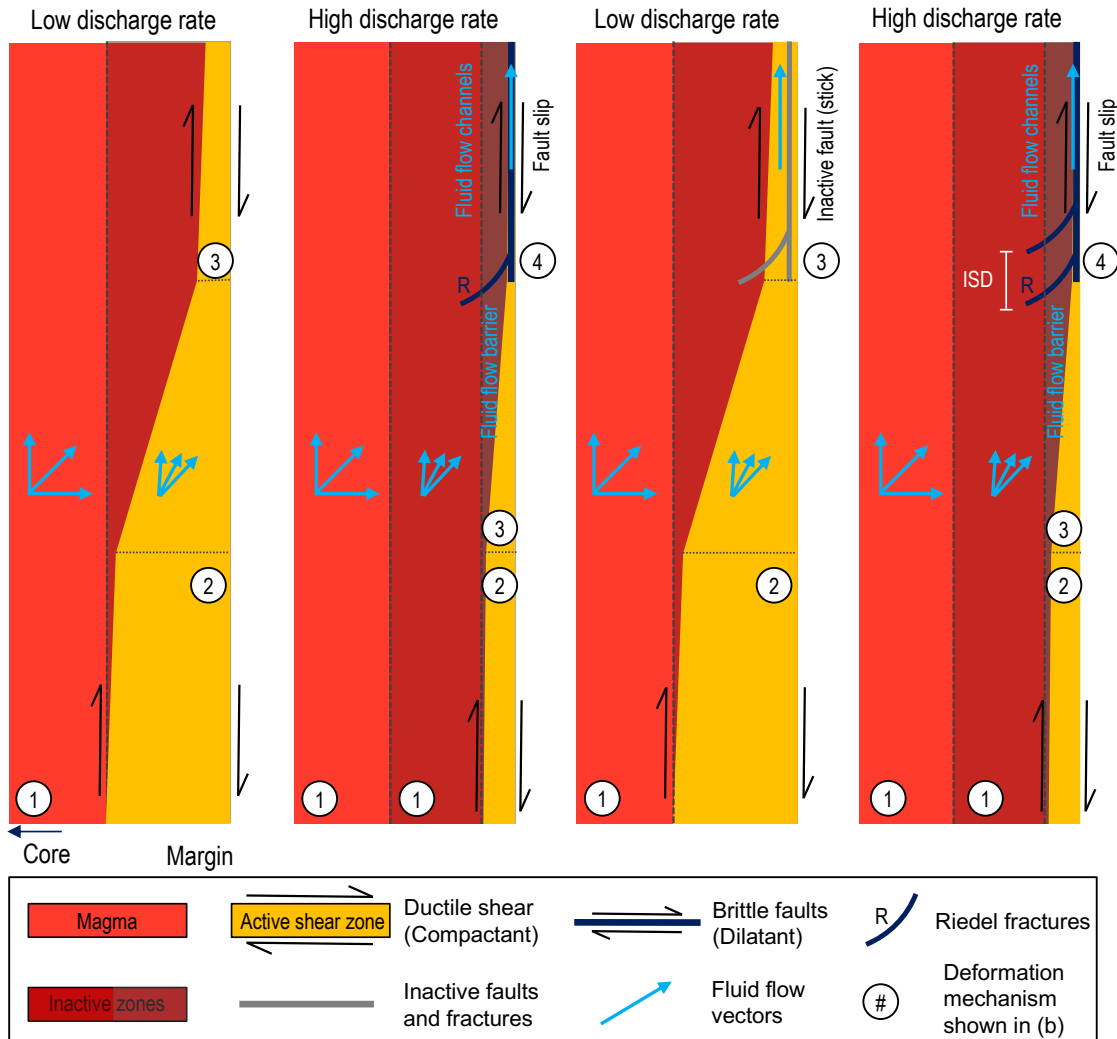


1392

1393

a

Shear and permeability evolution during pulsatory magma ascent



b

